Available online at www.sciencedirect.com

ScienceDirect

Geochimica et Cosmochimica Acta 71 (2007) 1764–1782

Geochimica et Cosmochimica Acta

www.elsevier.com/locate/gca

The partitioning behavior of As and Au in S-free and S-bearing magmatic assemblages

Adam C. Simon [a,*], Thomas Pettke [b], Philip A. Candela [c], Philip M. Piccoli [c], Christoph A. Heinrich [d]

[a] *Department of Geoscience, University of Nevada, Las Vegas, NV 89154-4010, USA*
[b] *Institute of Geological Sciences, University of Bern, Baltzerstrasse 1+3, CH-3012 Bern, Switzerland*
[c] *Laboratory for Mineral Deposits Research, Department of Geology, University of Maryland, College Park, MD 20742, USA*
[d] *Isotope Geochemistry and Mineral Resources, Department of Earth Sciences, Federal Institute of Technology, ETH Zentrum NO, CH-8092 Zurich, Switzerland*

Received 3 August 2006; accepted in revised form 2 January 2007; available online 10 January 2007

Abstract

The partitioning of As and Au between rhyolite melt and low-salinity vapor (2 wt% NaCl eq.) in a melt–vapor–Au metal ± magnetite ± pyrrhotite assemblage has been quantified at 800 °C, 120 MPa and $f_{O_2} = \text{NNO}$. The S-bearing runs have calculated values for the fugacities of H_2S, SO_2 and S_2 of $\log f_{H_2S} = 1.1$, $\log f_{SO_2} = -1.5$, and $\log f_{S_2} = -3.0$. The ratio of H_2S to SO_2 is on the order of 400. The experiments constrain the effect of S on the partitioning behavior of As and Au at magmatic conditions. Calculated average Nernst-type partition coefficients ($\pm 1\sigma$) for As between vapor and melt, $D_{\text{As}}^{\text{v/m}}$, are 1.0 ± 0.1 and 2.5 ± 0.3 in the S-free and S-bearing assemblages, respectively. These results suggest that sulfur has a small, but statistically meaningful, effect on the mass transfer of As between silicate melt and low-salinity vapor at the experimental conditions. Efficiencies of removal, calculated following Candela and Holland (1986), suggest that the S-free and S-bearing low-salinity vapor can scavenge approximately 41% and 63% As from water-saturated rhyolite melt, respectively, during devolatilization assuming that As is partitioned into magnetite and pyrrhotite during second boiling. The S-free data are consistent with the presence of arsenous acid, $As(OH)_3$ in the vapor phase. However, the S-bearing data suggest the presence of both arsenous acid and a As–S complex in S-bearing magmatic vapor. Apparent equilibrium constants, $\log K'_{\text{As}}(\pm 1\sigma)$, describing the partitioning of As between melt and vapor are −1.3 (0.1) and −1.1 (0.1) for the S-free and S-bearing runs, respectively. The increase in the value of K'_{As} with the addition of S suggests a role for S in complexing and scavenging As from the melt during degassing.

The calculated vapor/melt partition coefficients ($\pm 1\sigma$) for Au between vapor and melt, $D_{\text{Au}}^{\text{v/m}}$, in S-free and S-bearing assemblages are 15 ± 2.5 and 12 ± 0.3, respectively. Efficiencies of removal (Candela and Holland, 1986) for the S-free melt, calculated assuming that magnetite is the dominant Au-sequestering solid phase during crystallization (Simon et al., 2003), suggest that magmatic vapor may scavenge on the order of 72% Au from a water-saturated melt. Efficiencies of removal calculated for the S-bearing assemblage, assuming pyrrhotite and magnetite are the dominant Au-sequestering solid phases, indicate that vapor may scavenge on the order of 60% Au from the melt. These model calculations suggest that the loss of pyrrhotite and magnetite from a melt, owing to punctuated differentiation during ascent and emplacement, does not prohibit the ability of a rhyolite melt to generate a large-tonnage Au deposit. Apparent equilibrium constants describing the partitioning of Au between melt and vapor were calculated using the mean $D_{\text{Au}}^{\text{v/m}}$ values for the S-free and S-bearing assemblages; only S-bearing data from runs longer than 400 h were used as shorter runs may not have reached equilibrium with respect only to vapor/melt partitioning of Au. The values for $\log K'_{\text{Au}}(\pm 1\sigma)$ are −4.4 (0.1) and −4.2 (0.2) for the S-free and S-bearing runs, respectively. These data suggest that the presence of S does not affect the mass transfer of Au from degassing silicate melt to an exsolved,

---

[*] Corresponding author.
E-mail address: adam.simon@unlv.edu (A.C. Simon).

doi:10.1016/j.gca.2007.01.005

low-salinity vapor in a low-f_{S_2} assemblage (i.e., pyrrhotite–magnetite at NNO) at the experimental conditions reported here. Efficiencies of removal are calculated and used to model the mass transfer of Au from a crystallizing silicate melt to an exsolved, low-salinity vapor phase. The calculations suggest that the model, absolute tonnage of Au scavenged and transported by S-free and S-bearing vapors, from a crystallizing melt, would be comparable and that the time-integrated flux of low-salinity vapor could be responsible for a significant quantity of the Au in magmatic-hydrothermal ore deposits.

1. INTRODUCTION

Arsenic is a ubiquitous trace-element in active geothermal fluids (White, 1981; Stauffer and Thompson, 1984; Ballantyne and Moore, 1988; Price and Pichler, 2005) and volcanic gases (Symonds et al., 1990; Mambo et al., 1991; Symonds et al., 1992, 1994) and is often associated intimately with Au in subaqueous hot spring-type (Berger, 1985, 1986; Cunneen and Sillitoe, 1989), epithermal vein-type (Sillitoe, 1993a,b), Carlin-type (Hofstra and Cline, 2000; Cline et al., 2005) and porphyry-type (Heinrich et al., 1999) ore deposits. The association between As and Au in multiple ore deposit types and the commonly recognized presence of an As halo around many Au-rich epithermal- and porphyry-type ore bodies has led to As being labeled a "pathfinder" element in the search for high-grade Au deposits (Van Leeuwen et al., 1990; Cameron et al., 2002). In spite of the apparent strong relationship between the two metals in magmatic-hydrothermal ore deposits, there are few data constraining the behavior of As at the *PTX* conditions attending the evolution of silicate melts which supply the metals to the ore-forming environment and there are no data constraining the effects of S on metal partitioning.

Although some debate persists, there is ever-growing consensus that metals in epithermal- and porphyry-type ore deposits are derived from subjacent degassing silicate melt (Holland, 1972; Whitney, 1975; Burnham, 1979; Candela and Holland, 1984; Dilles, 1987; Hedenquist and Lowenstern, 1994; Audétat et al., 1998, 2000; Halter et al., 2005). The ability of a degassing melt to supply significant quantities of As and Au to the superjacent magmatic-hydrothermal environment via a magmatic volatile phase can be inferred from the high concentrations of As and Au in volcanic gas emissions (Symonds et al., 1987, 1990; Quisefit et al., 1989; Mambo et al., 1991; Mambo and Yoshida, 1993; Hedenquist et al., 1994; Hedenquist, 1995; Taran et al., 1995; Barnes and Seward, 1997; Fulignati and Sbrana, 1998; Signorelli et al., 1998; Yudovskaya et al., 2006). This is corroborated by in situ measurements of As distribution coefficients between melt and exsolving aqueous fluids from co-existing melt and fluid inclusion assemblages (Audétat et al., 2000; Audétat and Pettke, 2003). Importantly, the data from these studies evince that the As and Au concentrations in magmatic volatile phases may be amplified by several orders of magnitude relative to the their concentrations in the source melt.

The genetic link between a magmatic volatile phase(s) and Au- and As-mineralization is based on studies detailing the structural, fluid inclusion and isotopic evidence from mineralized zones and proximal igneous bodies (Emmons, 1927; Roedder, 1972, 1984; Burnham, 1979; Sillitoe, 1979, 1993a,b, 2000; Titley, 1981; Hedenquist, 1991; Richards et al., 1991; Vila and Sillitoe, 1991; Hedenquist et al., 1993, 1994; Hedenquist and Lowenstern, 1994; Arribas et al., 1995; Shinohara and Kazahaya, 1995; Gammons and Williams-Jones, 1997; Shinohara and Hedenquist, 1997; Audétat et al., 1998, 2000; Hedenquist et al., 1998; Heinrich et al., 1999; Cooke and Simmons, 2000; Marschik and Fontbote, 2001; Ulrich et al., 2001; Frank et al., 2002; Candela and Piccoli, 2005; Simmons et al., 2005). Fluid inclusions associated intimately with Au-ore mineralization in porphyry-type deposits offer the most convincing evidence that a magmatic volatile phase(s) evolved from intrusive magma may transport high concentrations of As and Au. Ulrich et al. (1999) report As and Au concentrations in fluid inclusions associated with ore mineralization at the Baja de la Alumbrera porphyry deposit, Argentina. The average Au concentration determined by Ulrich et al. (1999) in the presumed magmatic vapor is on the order of 0.5 μg/g. Arsenic was not quantified in the vapor inclusions. Assuming a Au concentration on the order of 0.1 μg/g in the parental melt at Bajo de la Alumbrera (Mustard et al., 2006) suggests a value for the vapor/melt partition coefficient for Au on the order of 5. These fluid inclusion data from porphyry-type ore deposits, coupled with chemical data from fumarole emissions, demonstrate that significant quantities of As and Au may be scavenged by magmatic volatile phases and transported into the overlying superjacent environment. The data from natural fluid inclusion assemblages (i.e., both vapor and brine) suggest that As and Au exhibit similar partitioning behavior at high temperature. However, only a small number of experimental studies have been performed to quantitatively evaluate the transport of Au at magmatic *PTX* conditions (Frank et al., 2002; Hanley et al., 2005; Simon et al., 2005) and there are no extant data constraining As behavior at magmatic conditions.

Frank et al. (2002) and Simon et al. (2005) report partition coefficients for Au in a S-free melt–brine assemblage at 800 °C and 100 MPa and melt–vapor–brine–magnetite assemblage at 800 °C and 100–145 MPa, respectively. Data from their studies demonstrate that at high activity of HCl in the volatile phase the concentration of Au in the volatile phase can be described by the equilibrium:

$$\mathrm{AuO}_{0.5}^{\mathrm{m}} + 2\mathrm{HCl}^{\mathrm{mvp}} = \mathrm{AuCl_2H}^{\mathrm{mvp}} + 0.5\mathrm{H_2O} \quad (1)$$

where MVP stands for magmatic volatile phase (i.e., vapor or brine). Data from Frank et al. (2002) suggest that Au solubility in the volatile phase is independent of chloride concentration in aqueous brine containing <11,000 μg/g HCl. Stefánsson and Seward (2003) demonstrate experimentally that Au solubility is independent of chloride concentration at pH > 5 over the temperature range 300–600 °C at 50–180 MPa. Thus, with increasing pH of the volatile phase the speciation of Au may transition from a gold(I) chloride complex to a gold(I) hydroxide complex during acid neutralization via the equilibrium:

$$AuOH^{mvp} + 2HCl^{mvp} = AuCl_2H^{mvp} + H_2O \tag{2}$$

The low solubility of Au as AuOH in experimental MVPs suggests that the shift from gold(I) chloride to gold(I) hydroxide complex during acid neutralization and cooling may be a contributing factor for significant Au precipitation from the aqueous fluid. However, while some Au loss may occur during acid neutralization, data from Stefánsson and Seward (2004) suggest that Au-speciation may transition from gold(I) chloride to gold(I) bisulfide with decreasing temperature. Their study demonstrates that in aqueous sulfide solutions, Au-speciation is dominated by AuHS at conditions up to 400 °C and 500 bar. At 500 bars, with increasing temperature from 350 to 500 °C the formation constant for AuHS decreases and Stefánsson and Seward (2004) postulate that gold(I) chloride and gold(I) oxide complex become important with increasing temperature. Even if gold(I) chloride and gold(I) oxide dominate Au-speciation, the data from Stefánsson and Seward (2004) combined with recent fluid inclusion data from natural systems (Heinrich et al., 1999; Ulrich et al., 1999) suggest that some Au may be transported as a gold–sulfur species at temperatures up to at least 650 °C and perhaps higher. Heinrich et al. (1999) and Ulrich et al. (1999) did not quantify directly the sulfur concentration of fluid inclusions, but rather infer the presence of Au–sulfur species based on volatility data from Drummond and Ohmoto (1985) as well as mass balance constraints for chlorine in vapor fluid inclusions in the boiling assemblage. At present, there are no experimental data which constrain the behavior of Au in a S-bearing melt–volatile phase system at temperatures above 500 °C and, thus, the effect of S on Au behavior at magmatic conditions remains unconstrained.

The experimental data constraining the behavior of As in magmatic-hydrothermal fluids is limited even further. Pokrovski et al. (2002a) report data which describe the partitioning of As between low-density vapor and high-density aqueous fluid at temperatures up to 500 °C and pressures up to 60 MPa. They demonstrate that the concentration of As in vapor is independent of both chloride and sulfide at concentrations up to 0.5 molal HCl or H_2S. They conclude that As speciation is dominated by arsenous acid, $As(OH)_3$, in both low-density vapor and dense NaCl–H_2O fluids. They conclude that $As(OH)_3$ is likely to be responsible for the preferential fractionation of As into the vapor phase in boiling assemblages described from porphyry-type ore deposit environments. A complementary study by Pokrovski et al. (2002b) elucidates the stability and solubility of arsenopyrite, FeAsS, in pure water and moderately acidic to slightly basic aqueous solutions with and without H_2 and/or H_2S at temperatures from 300 to 450 °C and pressures from 10 to 100 MPa. They report that the concentration of As in slightly acidic solutions equilibrated with FeAsS, with H_2 and H_2S buffered by the pyrite–pyrrhotite–magnetite assemblage, increases from 45 ± 15 to $24 \pm 2.2 \times 10^3$ μg/g as temperature and pressure increase from 300 °C and 40 MPa to 450 °C and 50 MPa. These data indicate that hydrothermal aqueous solutions may carry significant quantities of As at conditions relevant to the precipitation of metals in porphyry systems. Pokrovski et al. (2002b) suggest that the dissolution of arsenopyrite may act as a local reductant promoting the reduction of Au^{1+} in the aqueous fluid (present as $AuCl_2H$, AuOH and/or AuHS) to Au^0 and suggest that this may be the mechanism responsible for Au precipitation from ascending magmatic-hydrothermal fluids. If this hypothesis is correct, it may explain the commonly recognized occurrence of Au and arsenopyrite (and/or arsenian-pyrite) in epithermal, porphyry, and Carlin-type deposits (Fleet et al., 1993; Simon et al., 1999; Ye et al., 2003; Palenik et al., 2004; Cline et al., 2005). This brief discussion suggests that significant quantities of both As and Au may be transported in magmatic-hydrothermal volatile phases.

This paper presents experimental data which constrain the partitioning behavior of As and Au in a melt–vapor assemblage at high-temperature (800 °C) and pressure (120 MPa) in both a S-free and S-bearing (pyrrhotite) system. These data are the first step towards quantifying fully the relationship between As and Au in magmatic systems. Additional experiments quantifying the partitioning of As in a melt–vapor–brine ± FeAsS system at variable PT conditions are planned.

2. PROCEDURES

2.1. Starting materials

All experiments were performed in Au metal capsules (0.5 cm × 0.01 cm wall thickness × 3 cm length) imposing Au saturation (i.e., $a_{Au} = 1$) on the system. The starting melt is a synthetic haplogranite glass with the composition of a 100 MPa minimum melt, $Qz_{0.38}Ab_{0.33}Or_{0.29}$ on an anhydrous basis (Table 1). The starting S-free aqueous solution was prepared by adding reagent grade KCl, NaCl,

Table 1
Starting composition of synthetic haplogranite

Oxide	wt%
SiO_2	75.18
Al_2O_3	11.09
K_2O	4.43
Na_2O	3.67
CaO	0.17
Fe_2O_3	0.04
MnO	0.01
MgO	0.10
TiO_2	0.03
P_2O_5	0.03
LOI	4.51
Total	99.26

Chemical composition of the starting glass used in all experiments as determined by XRF. LOI, loss on ignition.

and HCl to doubly deionized-distilled water to yield a final aqueous salinity of 1.8 wt% NaCl eq. The salinity was chosen to lie in the brine-undersaturated vapor field of the NaCl–H_2O model system (Bodnar et al., 1985). Arsenous chloride (99.99% $AsCl_3$; Sigma–Aldrich) was used as the As-source in all S-free experiments. Arsenous chloride decomposes to yield $As(OH)_3$ in high temperature water vapor and the dissociated chloride complexes with hydrogen to yield HCl. Thus, the quantities of arsenous chloride and HCl added to the starting solutions were adjusted to ensure that the vapor at P and T contained a K:Na:H ratio close to unity. The lab water used to prepare starting solutions contains less than 0.1 μg/g As as determined by atomic absorption spectrophotometry. A volume of 0.5 mL arsenous chloride was added to a 100 mL volumetric flask yielding an As concentration of 4,465 ± 45 mg/L. The uncertainty reflects the estimated error in the volumetric pipette transfer (Eppendorf) and flask volume (Kimax). The flask volume was calibrated prior to use and was found to hold 100 ± 0.5 mL of lab grade water at 20 °C; calculated by using a density of water of 0.99821 g/cm^3 (CRC Handbook). The 500 μL volumetric pipette was calibrated and found to transfer 500 ± 1 μL (±0.2%) lab grade H_2O. Thus, the estimated error in the As concentration is assumed to be below 1%. The small quantity of As added to the starting solution prevents the dissociation of $AsCl_3$ and formation of solid arsenic trioxide (As_2O_3) at room temperature. Approximately 40 mg of haplogranite and 100 μL of NaCl–KCl–HCl–As(III)Cl-bearing aqueous solution were loaded into each capsule. This ratio was constant in all experiments.

The S-bearing experiments contained haplogranite (Table 1), arsenopyrite (FeAsS) and aqueous solution. Arsenic was not added to the starting solutions in the S-bearing experiments. Rather, approximately 1 mg of arsenopyrite was used as the As and S source in all S-bearing experiments. The arsenopyrite is ~100% end-member FeAsS as determined by electron probe microanalysis (EPMA). The starting solutions in the S-bearing runs contained only dissolved NaCl, KCl, and HCl at a molar ratio of Na:K:H of unity. The initial melt (40 mg) to aqueous fluid (100 μL ≈ 100 mg) to arsenopyrite (1 mg) mass ratio added to each capsule was held constant in all runs.

2.2. Experimental design

Loaded capsules were placed in dry ice and welded shut. Sealed capsules were weighed, then heated at 110 °C for a minimum of 4 h and re-weighed to verify mechanical integrity via no loss of mass. Individual capsules were placed inside René-41 pressure vessels along with a Ni filler rod. An air-driven water-pressure intensifier was used to impose pressure on the charge. Pressure was monitored with Bourdon-tube gauges (±2 MPa) which have been calibrated against factory-calibrated Heise gauges. Charges were first pressurized to 100 MPa and then left open to the water-pressure reservoir while heated to 800 °C inside doubly wound tube furnaces. Heating causes the pressure of the run to increase to near the final run pressure of 120 MPa. The furnaces were tilted such that the hot end of the vessel was maintained at a 10° angle from the horizontal bench upon which the furnace sits (Charles and Vidale, 1982). Temperatures were measured with type K (Chromel–Alumel) external thermocouples. The thermal gradient, determined in the presence of the water-pressure medium, is on the order of 1.3 °C per centimeter. The hot spot corresponds to the middle of the capsule and the temperature profile across the capsule is 797–798 °C at the cold end, 801–802 °C at the hot end and the mid-point of the capsule is 800 °C. The combination of a tilted vessel position, a Ni-filler rod and a low thermal gradient retards thermal convection in the charge which could otherwise inhibit the achievement of equilibrium.

Runs were terminated by removing the vessel from the furnace and blowing a high-pressure air stream across the vessel to cool it from 800 to 200 °C over approximately 2 min followed by immediate immersion in an ambient-temperature water bath. Capsules were removed from the vessels, cleaned, and weighed to determine if the capsules remained mechanically closed during the experiment. Only capsules that exhibited no mass change (±3 mg) were processed for analysis. All capsules were opened under a negative-pressure fume hood to avoid inhalation of volatile arsenic compounds.

2.3. Control of the fugacities of O_2, H_2, S_2, H_2S, and SO_2

The fugacity of oxygen in all experiments was controlled intrinsically at the nickel–nickel oxide (NNO) oxygen fugacity buffer by the combination of thermal dissociation of the water pressure medium, reaction of oxygen with the nickel pressure vessel and hydrogen diffusion through the Au capsule walls. The diffusion of hydrogen through the Au capsule walls and the establishment of osmotic equilibrium between the charge and the pressure buffer imposes a hydrogen fugacity on the charge equal to NNO (Chou, 1987a). We verified experimentally that the f_{O_2} = NNO ($\log f_{O_2}$ is -14 ± 1.0) by using the hydrogen sensor technique (Ag–AgCl; H_2O–AgCl) described by Chou (1987a). A value for f_{H_2} of 5.8 bars was calculated by using the equations of Huebner and Sato (1970) and Belonoshko et al. (1992). The fugacities of oxygen, f_{O_2}, and hydrogen, f_{H_2}, were used to calculate the fugacity of water, f_{H_2O}, by using the equilibrium constant:

$$K_w = \frac{f_{H_2} \times (f_{O_2})^{0.5}}{f_{H_2O}} \tag{3}$$

With a total salinity on the order of 2 wt% NaCl eq. and H_2 and H_2S pressures less than 50 bars, the partial pressure of H_2O will be close to the total pressure. At this pressure, the fugacity of pure H_2O is on the order of 10^3. The model of Clemente et al. (2004) was used to calculate the fugacities of hydrogen, sulfur, sulfur dioxide, and hydrogen sulfide in S-bearing experiments. Their model calculates f_{H_2}, f_{S_2}, f_{H_2S}, f_{SO_2} at fixed P, T, sulfur concentration of the glass, f_{O_2} and f_{H_2O}. The f_{H_2O} obtained by using the Burnham (1979) model was used in the calculations. The modified Redlich–Kwong equation of state (MRK-EOS) of Holloway (1977) is built into the model to calculate f_{S_2}. The f_{S_2} is constrained to lie along the magnetite–pyrrhotite curve (based on the presence of both phases in run products) at a fixed f_{O_2}. Once f_{S_2}, f_{H_2} and f_{O_2} are determined, the values for f_{H_2S} and f_{SO_2} are calculated by using the following equilibrium constants provided in Ohmoto and Kerrick (1977):

$$K_{H_2S} = \frac{f_{H_2S}}{f_{S_2} \times f_{H_2}} \tag{4}$$

$$\text{and } K_{SO_2} = \frac{f_{SO_2}}{f_{O_2} \times f_{S_2}}. \tag{5}$$

The calculated volatile fugacities are: $\log f_{O_2} = -13.9$; $f_{H_2} = 5.8$; $\log f_{S_2} = -3.0$; $\log f_{H_2S} = 1.1$ and $\log f_{SO_2} = -1.5$.

2.4. Run-product description

The S-free run-products consist of glass (i.e., quenched melt) and aqueous fluid. Glass was recovered as a single bead from all runs. Petrographic examination of the glass from each run indicates that it contains primary fluid inclusions trapped as the melt passed through the glass transition temperature during quench (Fig. 1). Individual fluid inclusions range in size from ~10 to ~100 µm with the majority of fluid inclusions in the 10–30 µm range. The glass-hosted fluid inclusions trap a direct sample of the low-salinity aqueous fluid phase which was in intimate contact with the melt at run conditions. The phase assemblage at run conditions was silicate melt, vapor, magnetite and pyrrhotite. As the melt was completely fluid until quench there is no possibility of forming secondary or pseudo-inclusions both of which require the presence of fractures in a solid medium. The fluid inclusions contain a vapor bubble and liquid at room temperature. The liquid–vapor phase proportions are consistent in fluid inclusions from all runs. No halide crystals were observed in any fluid inclusions indicating that the salinity of the volatile phase remained in the brine-undersaturated vapor-only field at run conditions. The new results presented here, at the experimental conditions outlined in Sections 2.1–2.3, are consistent with known phase relations for NaCl–KCl–H_2O aqueous fluids (Bodnar et al., 1985; Chou, 1987b; Sterner et al., 1989; Chou et al., 1992).

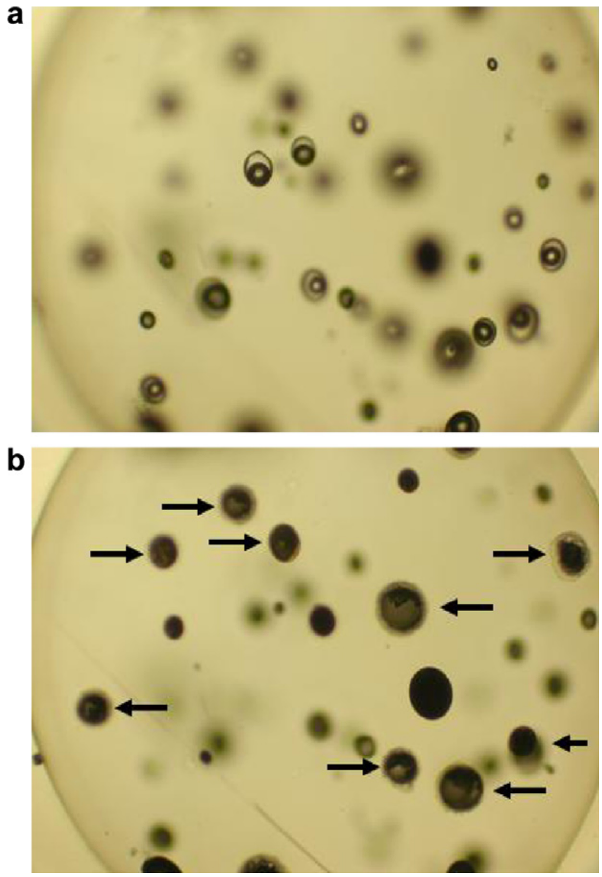

Fig. 1. Photomicrographs of glass and glass-hosted vapor fluid inclusions. Field of view is approximately 1.5 mm across in both photomicrographs. Note the spherical outline of the glass bead. Photo (a) is focused on a plane approximately 50 µm beneath the glass surface to show fluid inclusions hosted in the glass. Photo (b) is focused on the glass surface after LA-ICPMS analyses; the laser pits are marked by arrows.

The run-products of S-bearing charges consist of glass, aqueous fluid, and opaque solids. The glasses contain aqueous fluid inclusions consisting of a vapor bubble and liquid. The vapor bubble and liquid phase proportions are visually constant among all fluid inclusions in a given glass and among glasses from all runs. No halide crystals were observed in any glass-hosted fluid inclusion. The opaque phases in S-bearing glasses are magnetic and are interpreted to be pyrrhotite and magnetite based on petrographic high power (500×) observation of hexagonal and cubic crystals, respectively. The apparent absence of arsenopyrite in all run-products is consistent with phase equilibrium studies in the Fe–As–S system by Barton (1969) and Clark (1960). Their studies demonstrate that FeAsS in equilibrium with vapor is stable at high temperatures (>700 °C) only at As-rich compositions between approximately 75 and 80 atomic % As (when projected along the S–As binary in the Fe–As–S ternary system). The reaction of FeAsS with the volatile phase decreases the As content of arsenopyrite and results in the formation of pyrrhotite and magnetite. Thus, the assemblage melt–vapor–pyrrhotite–magnetite is the stable phase assemblage in the S-bearing runs.

2.5. Demonstration of equilibrium

The partitioning behavior of As and Au in melt–vapor experiments remains relatively constant over run durations varying from 187 to 1192 h. The magmatic vapor at run PTX conditions was sampled by trapping the vapor in glass-hosted fluid inclusions as the melt passed through the glass transition temperature. The time to cool from run temperature through the glass transition temperature (T_g) is on the order of 35 s and, as discussed below, consistent fluid inclusion salinities and major and minor element concentrations data from this study suggest that the trapping of vapor fluid inclusions is rapid enough to prevent statistically significant modification of the vapor chemistry. The T_g for water-saturated haplogranite is on the order of 400 °C (Dingwell, 1998, 2003; Sowerby and Keppler, 1999). The time invariance of the partitioning data, discussed below, is inferred to reflect the achievement of equilibrium between the vapor and melt at run conditions. This conclusion agrees with previous studies involving melt–volatile phase equilibria (Candela and Holland, 1984; Frank et al., 2002; Simon et al., 2004, 2005).

2.6. Analytical procedures

2.6.1. *Analyses of experimental glasses*

The major element, Cl and S concentrations of run-product silicate glasses were quantified by using a JEOL JXA 8900 EPMA. Glass samples were mounted, polished with diamond paste and coated with a ~0.03 μm carbon film. Operating conditions for glass analyses for major elements and Cl were a 5 nA beam current, 15 keV accelerating potential, and a 15 μm beam size. A minimum counting time of 20 s (sum of peak and background) was used for each spot analysis. Line traverses with fifteen spot analyses were performed to evaluate melt homogeneity (i.e., rim to core to rim). Sulfur was analyzed by using WDS with a PET crystal and the following probe conditions: a 10 nA beam current, 15 keV accelerating potential and a 10 μm defocused beam counting on S for 100 s and background for 50 s on either side of the S peak. Higher cup currents were not used as this would result in rapid diffusion of Na and potentially Cl and S. The reportable detection limit for S is 150 μg/g. Chlorine and Na were also analyzed simultaneously with S. Analyses yielding anomalously high Cl and Na concentrations were interpreted to represent the presence of a fluid inclusion and were eliminated from the data set. Replicate analyses indicated that there was no observable migration of sodium in the glass as discussed in Morgan and London (1996) and Acosta-Vigil et al. (2003). Yellowstone rhyolite (National Museum of Natural History, NMNH 72854 VG568) was used to standardize for Si, Al, Na, and K. Kakanui hornblende was used as the standard for Fe. Scapolite (Meionite, Brazil, USNM R6600-1) was used to standardize for Cl. Pyrite was used to standardize for S. Detailed information for standards is located at http://nvl.nist.gov/pub/nistpubs/jres/107/6/j76jar.pdf.

The As and Au concentrations of silicate glass were quantified by using LA-ICPMS with the setup used for fluid inclusions described below. Spot sizes of 75, 80, 90 or 100 μm spot size were used to ablate glass volumes petrographically devoid of fluid inclusions and crystals; four to six large-beam analyses were performed on each glass. Additionally, the As and Au concentrations of glass volumes directly above and below analyzed fluid inclusions were quantified. Thus, the data reported here reflect 12–18 glass analyses per experiment. Transient analytical signals were integrated and isotope sensitivity ratios were calculated by using the NIST SRM-610 glass. Absolute element abundances were calculated by using the EPMA-determined Al concentration as the internal standard.

2.6.2. *Fluid inclusion microthermometry*

Microthermometry was performed on fluid inclusions hosted in the same glass aliquot analyzed by EPMA. Following EPMA, the carbon coat was removed by diamond polishing and the probe mounts were cut into wafers on the order of 500–1000 μm thick to expose glass on the top and bottom sides of each wafer. The top and bottom of each glass disc were polished with successively finer grit diamond paste and alumina and agitated ultrasonically for ten minutes in cold, lab-grade H_2O prior to microthermometric analysis. A USGS-type, gas-flow heating-freezing stage (Fluid, Inc.) was used to measure T_{mice}. The thermocouple was placed directly on top of the sample to prevent sample movement and to minimize the distance between the thermocouple and fluid inclusions; both serve to decrease uncertainties in temperature measurements. The heating-freezing stage was calibrated at −56.6 °C (the melting temperature of pure solid CO_2) and 0 °C (the melting temperature of pure H_2O). The salinities of vapor inclusions were calculated by using the ice melting temperatures (i.e., T_{mice}) and the equations of Bodnar and Vityk (1994). Measurement uncertainties in final ice melting temperatures are ±0.2 °C. Inclusions analyzed throughout the melt volume indicate that salinity gradients are absent. Repeated cycling of inclusions through their T_{mice} indicate that the volume, estimated visually by using the micrometer scale in the ocular, and the measured T_{mice}, did not vary as a result of freezing and heating. Thus, we conclude that no change in salinity of the fluid inclusions occurred owing to the loss of water through bulk or surface diffusion during microthermometric measurements.

2.6.3. *LA-ICPMS analyses of synthetic fluid inclusions*

The concentrations of As, Au, Na, K, and Fe in individual fluid inclusions were quantified by LA-ICPMS. The LA-ICPMS system is equipped with an energy-homogenized (Microlas) pulsed 193-nm ArF Excimer laser (Compex 102, Lamda Physik) that allows controlled ablation (Günther et al., 1997, 1998; Heinrich et al., 2003). Quadrupole ICPMS (Elan 6100, Perkin-Elmer) settings were similar to those reported in Pettke et al. (2004). The diameter of the laser beam was set slightly greater than the maximum diameter of each fluid inclusion so that the entire fluid inclusion was ablated together with a minimal volume of surrounding matrix glass. The mass of glass co-ablated with the fluid inclusion does not affect the reported concentrations of elements in the fluid inclusion (Heinrich et al., 2003). Short dwell times per isotope were used to ensure representative sampling of the short, transient signals (Pettke et al., 2000) notably from glass-hosted inclusions. Microthermometrically determined Na concentrations of each ablated fluid inclusion were used as the internal standard to calculate absolute element concentrations in the fluid inclusion. Data reduction techniques are described in detail in Heinrich et al. (2003) and the use of Na as the internal standard is discussed in Heinrich et al. (1992) and Simon et al. (2007).

3. RESULTS

3.1. Metal concentrations in vapor and melt

3.1.1. *Haplogranite melt*

The major element, Cl and S concentrations of S-free and S-bearing glasses are presented in Table 2. The data

Table 2
EPMA analyses of major elements, chlorine and sulfur in the run product glasses

Run number	Run time (h)	SiO_2 wt% $(\pm 1\sigma)$	K_2O wt% $(\pm 1\sigma)$	Na_2O wt% $(\pm 1\sigma)$	FeO wt% $(\pm 1\sigma)$	Al_2O_3wt% $(\pm 1\sigma)$	Cl wt% $(\pm 1\sigma)$	S µg/g[a] $(\pm 1\sigma)$	Total $(\pm 1\sigma)$	ASI
S-free runs										
As-7	933	74.86 (0.19)	4.64 (0.03)	3.40 (0.05)	0.03 (0.02)	11.38 (0.08)	0.11 (0.003)	BD[b]	94.44 (1.00)	1.07
As-8	1192	75.20 (0.12)	4.51 (0.05)	3.17 (0.05)	0.06 (0.02)	11.02 (0.05)	0.11 (0.003)	BD[b]	94.10 (1.28)	1.09
As-9	457	75.51 (0.17)	4.72 (0.04)	3.22 (0.04)	0.20 (0.03)	11.20 (0.11)	0.11 (0.004)	BD[b]	94.02 (0.95)	1.09
As-10	1000	74.79 (0.18)	4.46 (0.03)	3.45 (0.03)	0.07 (0.02)	11.26 (0.05)	0.12 (0.005)	BD[b]	94.17 (1.43)	1.07
As-11	353	74.49 (0.15)	4.74 (0.05)	3.08 (0.04)	0.98 (0.02)	10.91 (0.10)	0.12 (0.003)	BD[b]	93.49 (1.33)	1.13
Mean		74.97 (0.20)	4.16 (0.06)	3.26 (0.08)	0.27 (0.20)	11.15 (0.09)	0.11 (0.003)	BD[b]	94.04 (0.17)	
S-bearing runs										
As-19	318	74.83 (0.19)	4.37 (0.05)	3.16 (0.06)	0.30 (0.04)	11.05 (0.14)	0.09 (0.005)	189 (38)	93.83 (1.13)	1.02
As-21	187	75.40 (0.16)	4.83 (0.03)	3.15 (0.06)	0.38 (0.07)	11.02 (0.13)	0.09 (0.004)	160 (8)	94.89 (1.30)	1.06
As-22	222	74.61 (0.39)	4.79 (0.06)	3.01 (0.13)	0.47 (0.05)	11.07 (0.24)	0.10 (0.005)	BD[b,c]	94.57 (1.34)	1.09
As-23	397	74.16 (0.21)	4.87 (0.05)	3.23 (0.06)	0.43 (0.05)	11.49 (0.16)	0.10 (0.003)	BD[b,d]	94.26 (1.07)	1.09
As-25	689	74.81 (0.25)	4.88 (0.04)	3.25 (0.06)	0.51 (0.11)	11.33 (0.14)	0.12 (0.006)	164 (30)	94.90 (1.48)	1.07
As-26	936	74.45 (0.19)	4.94 (0.04)	3.45 (0.04)	1.26 (0.08)	11.54 (0.12)	0.15 (0.009)	178 (17)	95.76 (1.35)	1.05
Mean		74.68 (0.21)	4.86 (0.02)	3.22 (0.07)	0.61 (0.16)	11.29 (0.11)	0.11 (0.01)	BD[b,e]	94.88 (0.25)	

Each datum represents the average of a minimum of fifteen spot analyses in different areas of a given experimental glass. ASI was calculated as the molar ratio $[Al_2O_3/(Na_2O + K_2O)]$. The calculated values of ASI indicate that all experimental melts were peraluminous. Uncertainties are presented as the standard deviation from the mean $(\pm 1\sigma)$.

[a] The reportable detection limit for S is 150 µg/g.

[b] BD, below detection.

[c] The concentration of S in this glass is 68 ± 22 µg/g, below the reportable detection limit (RDL).

[d] The concentration of S in this glass is 108 ± 38 µg/g, below the RDL.

[e] The concentration of S in this glass is 144 ± 6 µg/g, below the RDL.

demonstrate that the silicate glasses from individual runs are homogeneous with respect to all elements. All glasses are mildly peraluminous with values for the aluminum saturation index (ASI = the molar ratio of $Al_2O_3/Na_2O + K_2O$) ranging from 1.07 to 1.13 in the S-free runs and 1.02 to 1.09 in the S-bearing runs. EPMA oxide plus Cl totals are on the order of 94 wt% which is consistent with the expected solubility of water in the melt of approximately 5–6 wt% H_2O. The concentration of major elements, Cl and S remains unchanged with run times from 187 to 1000 h suggesting that the melts achieve equilibrium with respect to major elements, Cl and S in less than 7 days, consistent with data from other studies (Carmichael and MacKenzie, 1963; Thompson and MacKenzie, 1967; Bailey et al., 1974; Bailey and Cooper, 1978; Baker and Rutherford, 1996; Gaillard et al., 2001; Scaillet and MacDonald, 2001; Clemente et al., 2004).

The concentrations of As and Au in glass are reported in Table 3. In most cases, the reported As and Au concentrations were calculated by using intensities averaged over the entire LA-ICPMS transient signal. Fig. 2 shows a LA-ICPMS signal which displays homogeneous As and Au intensities throughout the ablated volume of glass. This transient signal is characteristic for most analyses of glass. However, on the order of 10% of all transient signals display strong jumps in the intensities of Au and, in some cases, As. The presence of Au–As intensity jumps was noted only a few times among all analyses. The presence of Au intensity jumps is more common. Fig. 3a shows a characteristic LA-ICPMS signal for glass analyses which display jumps in As and Au intensities; that is the signal reveals a heterogeneous distribution of Au and As in glass. The apparent Na peak at ~110 s in Fig. 3a does not reflect the presence of a fluid inclusion. Fig. 3b is a blowup of the time period from 105 to 115 s. The signal for K has been added to Fig. 3b to illustrate that there is no fluid inclusion associated with the As and Au jumps at 110 s. The heterogeneity in As (110 s) and Au (59 and 120 s) displayed in Fig. 3a represents either (1) metal particles which were present as stable phases at run conditions or (2) metal particles which precipitated during quench and were subsequently trapped in the glass. The presence of these particles presents a challenge during data reduction. If the particles are treated as stable phases at run conditions and not regarded as part of the melt, their removal during signal processing results in a calculated metal concentration which is lower than that calculated by treating the particles as quench phenomena. As such, it is instructive to consider potential mechanisms of particle formation and evaluate their effect on the data reported here.

The presence of Au particles in experimentally produced silicate glasses was noted by Frank et al. (2002) based on their interpretation of secondary ion mass spectrometry (SIMS) analyses of Au-saturated haplogranite at 800 °C and 100 MPa. They hypothesized that the particles represented Au which precipitated from the melt during quench as the melt cooled from run temperature through the T_g. As the solubility of Au in the melt is expected to drop with decreasing temperature, the effect of cooling the melt several hundred degrees through the T_g could allow the "excess" Au to exsolve from the melt and form free Au particles. The signal shown in Fig. 3 is from a glass analysis of run As-25.

Table 3
LA-ICPMS data for glass and glass-hosted vapor fluid inclusions

Run No.	Type of inclusions analyzed	Number of inclusions analyzed[a]	Final wt% NaCl eq.[b]	Final HCl μg/g (±1σ)[c]	As in glass μg/g (±1σ)	As in fluid inclusions μg/g (±1σ)	Au in glass μg/g (±1σ)	Au in fluid inclusions μg/g (±1σ)
S-free runs								
As-7	Vapor	9	1.5–1.9	3700 (519)	511 (27)	329 (141)	2.0 (0.5)	30 (7)
As-8	Vapor	10	1.4–1.8	3635 (406)	365 (12)	335 (64)	1.6 (0.5)	28 (2)
As-9	Vapor	10	1.6–1.9	3963 (436)	179 (20)	195 (50)	1.1 (0.2)	23 (5)
As-10	Vapor	10	1.5–1.8	2786 (395)	307 (45)	358 (114)	3.0 (1.0)	39 (8)
As-11	Vapor	10	1.3–2.0	2938 (438)	433 (43)	415 (91)	4.7 (0.6)	28 (4)
Mean				3404 (256)	359 (63)	323 (44)	2.5 (0.7)	30 (3)
S-bearing runs								
As-19	Vapor	10	1.6–2.0	3031 (469)	357 (60)	500 (44)	0.36 (0.21)	7 (3)
As-21	Vapor	8	1.5–1.9	2319 (619)	307 (34)	793 (90)	0.40 (0.22)	10 (7)
As-22	Vapor	8	1.6–1.9	3357 (596)	438 (36)	1173 (142)	0.89 (0.48)	28 (4)
As-23	Vapor	8	1.3–2.0	3555 (639)	464 (54)	1109 (73)	0.18 (0.12)	9 (3)
As-25	Vapor	8	1.4–1.8	2803 (649)	335 (113)	627 (47)	1.1 (0.48)	13 (2)
As-26	Vapor	7	1.5–2.0	2030 (617)	198 (80)	681 (139)	0.53 (0.23)	6 (3)
Mean				2850 (264)	350 (43)	814 (121)	0.60 (0.16)	12 (4)

[a] Twenty fluid inclusions were microthermometrically analyzed in the glass run product from each experiment. Of the total number of fluid inclusions analyzed microthermometrically, only about half were analyzed by LA-ICPMS.

[b] Final salinities are the range for all twenty fluid inclusions measured from the glass.

[c] HCl concentrations were calculated following Williams et al. (1997) with uncertainties calculated by using the general error propagation formula. Run times provided in Table 2.

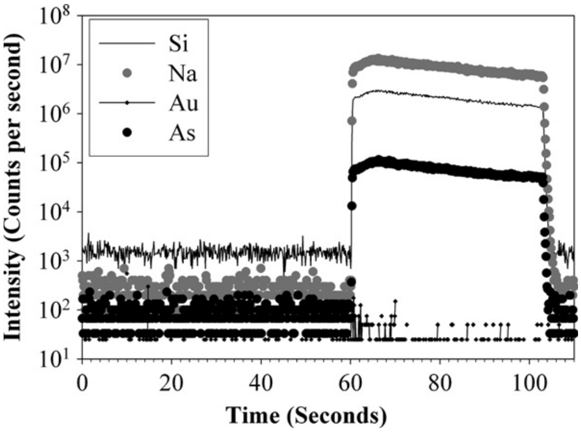

Fig. 2. LA-ICPMS transient signal of a glass analysis (shot my11a03). A laser spot size of 75 μm was used to ablate the glass. The intensities for all elements are homogeneous throughout the glass volume.

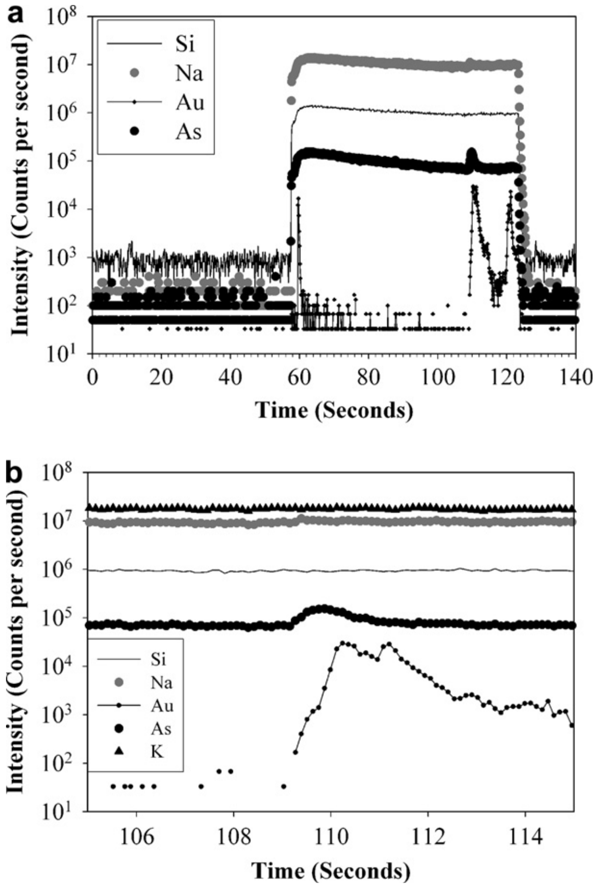

Fig. 3. (a) LA-ICPMS transient signal of a glass analysis (shot ma11a08). A laser spot size of 75 μm was used to ablate the glass. The intensities for Au and As exhibit jumps at approximately 60, 110 and 122 s. The intensity jumps at 60 and 122 s are interpreted to reflect the presence of Au particles in the glass. The intensity jump at 110 s reflects the presence of a As–Au alloy particle in the glass. These particles were most likely exsolved from the melt and trapped as the melt cooled through the glass transition temperature. (b) The signal from Fig. 3a focusing only on the time interval for the Au–As nugget ablated between 105 to 115 s. The signal for K has been added to highlight that the increase in the Au and As intensities are not correlated with an increase in either Na or K.

Treating the particles as quench phenomena and integrating over the entire glass signal from 58 to 122 s yields Au and As concentrations of 2.3 and 463 μg/g, respectively. If the intensity jumps for Au (at 60 and 120 s) and Au–As (at 110 s) are treated as alloys which were stable phases at run conditions and, thus, removed from the signal, the calculated Au and As concentrations are 0.124 and 459 μg/g, respectively. These results indicate that eliminating the Au–As alloy at 110 s does not affect statistically the calculated concentration of As. The concentration of Au, however, decreases by one order of magnitude if the Au particles are removed from the signal. Thirteen separate spots on the polished glass surface (As-25) were analyzed: two locations with a 100 μm laser spot size, three locations with a 90 μm laser spot size, three locations with a 80 μm laser spot size, and five locations with a 75 μm laser spot size. The average Au concentration ($\pm 1\sigma$) calculated from all the laser shots, without removing any visually obvious particles, is 1.1 ± 0.48 μg/g. Despite the high uncertainty and implied heterogeneity with respect to Au, this datum agrees well with the range of 2–4 μg/g reported by Jugo et al. (1999) for Au solubility in a S-bearing rhyolite at 850 °C and 100 MPa. Jugo et al. (1999) quantified Au solubility using Instrumental Neutron Activation Analysis (INAA) which is a bulk analytical technique that does not allow one to decipher the presence of Au particles. Other studies have also reported Au solubility values on the order of 0.5–1 μg/g in S-free haplogranite (Frank et al., 2002; Simon et al., 2003), consistent with the data reported here. Removing the visually obvious Au nuggets from transient signals for As-25 results in a calculated Au solubility ($\pm 1\sigma$) of 0.10 ± 0.04 μg/g. This solubility value is lower than, albeit consistent with, the solubility value of 0.5 reported by Simon et al. (2003), but is lower by one order of magnitude than Au solubility data reported by Jugo et al. (1999) and Frank et al. (2002).

Gold metal capsules serve as the source of Au in all runs and Au is delivered to the melt via diffusion directly from the capsule to the melt where these two media are in physical contact and via diffusion of Au from the capsule to the melt via the vapor phase. The ability of the melt to equilibrate with respect to Au can be tested by considering the amount of time required for Au to diffuse through the entire melt volume at run conditions. There are no data in the literature which constrain the diffusion of Au in hydrous silicate melts; however, diffusion data for the univalent metals Na and Cs in water-saturated granite melts at 800 °C (Watson, 1994) can be used to approximate a reasonable diffusion coefficient for Au. Watson (1994) reports diffusion coefficients of approximately $10^{-9.5}$ m^2 s^{-1} and 10^{-12} m^2 s^{-1} for Na and Cs, respectively. Univalent Au has a radius that is approximately halfway between those of Na and Cs and, thus, a reasonable estimate for the diffusion coefficient of Au is 10^{-11} m^2 s^{-1}. Using this diffusion coefficient value suggests that Au diffuses 2 mm over the first 100 h of run time. The glass beads recovered from all experiments have diameters on the order of 2 mm which suggests that the melts should have reached diffusional equilibrium within the first one hundred hours. This timescale is consistent with data for major elements as can be gleaned in Table 2.

The existence of free Au particles in the melt at run conditions requires a driving force for their formation. The runs described herein are isobaric and isothermal, with thermal gradients on the order of 1.3 °C/cm, which yields a total temperature difference of no greater than 0.2 °C across the 2 mm diameter melt. In the absence of strong gradients in temperature, there is no obvious mechanism for the growth and stability of free Au in the melt at run conditions and, thus, it is considered unrealistic for the particles to have existed in the melt as stable phases at run conditions. Alternatively, the effect of decreasing Au solubility in the melt during quench has the potential to affect significantly the stability of Au in the melt and potentially promote the nucleation and growth of Au particles as the melt cools through the glass transition temperature.

The experiments in this paper were quenched from 800 to 400 °C over a total time of 35–40 s, resulting in a quench rate of approximately 10 °C s^{-1} through the T_g. The question then is whether or not a Au particle can nucleate from the melt and scavenge sufficient Au, via diffusion of Au through the melt to the exsolved Au particle, to form particles of the size displayed in Fig. 3. Using the value for Au diffusion of 10^{-11} $m^2\ s^{-1}$ and a time of 40 s from run temperature (800 °C) to the T_g (400 °C) yields a diffusion distance of 20 μm from run temperature through the T_g. This implies that a nucleated Au particle may scavenge Au from a spherical volume of approximately 3.2×10^4 rμm^3 ($4 \times x^3$ with $x =$ diffusion length). The transient signal displayed in Fig. 3 is from an analysis which involved the ablation of a total glass volume on the order of 5.3×10^5 μm^3 (75 μm beam diameter, 120 μm pit depth; $\pi \times r^2 \times h$). The particles at 58, 110, and 122 s in Fig. 3a are ablated over 2, 5, and 4 s, respectively, corresponding to maximum long dimensions on the order of 4, 10, and 8 μm based on the drilling rate of 2 μm per second. We have tried to use back-scattered-electron (BSE) imaging to identify nuggets in the glass, but have been unsuccessful. The nuggets identified in the LA-ICPMS signals are ablated from within the glass matrix and, thus, these nuggets are not at the surface. Observing nuggets at the surface would require the random chance that nuggets would be polished directly at the surface. In the future, I plan to use secondary ion mass spectrometry (SIMS) depth-profiling to study these glasses, but this is beyond the scope of the present study. The calculated Au scavenging potential of each particle suggests that heterogeneous nucleation of Au particles during quench can result in the formation of Au nuggets which display transient intensities several orders of magnitude greater than the background glass. Thus, without data to support the hypothesis that the particles were stable phases at run conditions, we conclude that the Au particles are quench phenomena. Thus, transient signals from all runs were integrated over the entire signal without filtering them for nuggets. While this results in relatively high uncertainties owing to the heterogeneous growth of Au particles during quench, the Au solubility values reported here are comparable to those reported in other studies (Jugo et al., 1999; Frank et al., 2002; Simon et al., 2005) and we interpret the consistency between micro-analytical techniques such as LA-ICPMS (this study, Simon et al., 2003, 2005) and SIMS (Frank et al., 2002) and bulk analysis techniques such as INAA (Jugo et al., 1999; Frank et al., 2002) to indicate that the new data provide a reasonable estimate for Au solubility in S-free and S-bearing haplogranite.

3.1.2. *Glass-hosted vapor fluid inclusions*

The concentrations of As and Au in aqueous vapor are presented in Table 3. The HCl concentration of the vapor phase in each run, calculated following Williams et al. (1997), is on the order of 0.1 molal. The salinity values reported are the range for all fluid inclusions in each run; at least 20 inclusions in each glass were analyzed microthermometrically. The consistent fluid inclusion salinities throughout each glass indicate that salinity gradients were absent at run conditions; this is expected for an isobaric and isothermal system. Extant data for the analogue H_2O–NaCl–KCl–HCl ± $FeCl_2$ system indicate that brine-undersaturated vapor in equilibrium with haplogranite at 120 MPa and 800 °C should have a salinity < 3 wt% NaCl eq. (Sourirajan and Kennedy, 1962; Bodnar et al., 1985; Chou, 1987b; Chou et al., 1992; Sterner et al., 1992; Anderko and Pitzer, 1993). The lack of observed brine inclusions and the range of final salinities, on the order of 1.3–2 wt% NaCl eq., indicate that the runs were brine-undersaturated. A comparison of the vapor salinities in the S-free and S-bearing runs indicates that the addition of sulfur to the vapor does not cause statistically detectable changes in the measured vapor salinities.

A representative LA-ICPMS transient signal from a fluid inclusion analysis is presented in Fig. 4a. The fluid inclusion signal is shown again in Fig. 4b with a focus only on the ablated fluid inclusion. Note that the intensities for Na, As, and Au all climb together from background levels at 91.8 s, exhibit a maximum in intensity at 92.1–92.5 s and then all three elements display parallel decays to background intensities by 93.1 s. This signal suggests that Au is part of the solute load of the fluid inclusion.

The data presented in Table 3 indicate that Au concentrations in S-bearing fluid inclusions are lower and more variable relative to Au concentrations in the S-free vapor inclusions. Some LA-ICPMS signals for S-bearing fluid inclusions display anomalous jumps in the intensity of Au that coincide with the ablation of the targeted fluid inclusion. These intensity jumps are interpreted to reflect the presence of a Au particle trapped at the interface between glass and the targeted vapor inclusion. These particles may act as a nucleus and seed the formation of a fluid inclusion in the glass. One example analysis is provided in Fig. 5a. Fig. 5b is a blow-up of only the ablation interval for the fluid inclusion. The vapor fluid inclusion was ablated between 66.2 and 68 s as noted by the sharp rise and fall in Na and As intensities during this time interval. The intensity for Au increases at approximately 66.2 s which seemingly indicates that it belongs to the fluid inclusion. However, the magnitude of the Au intensity exceeds that

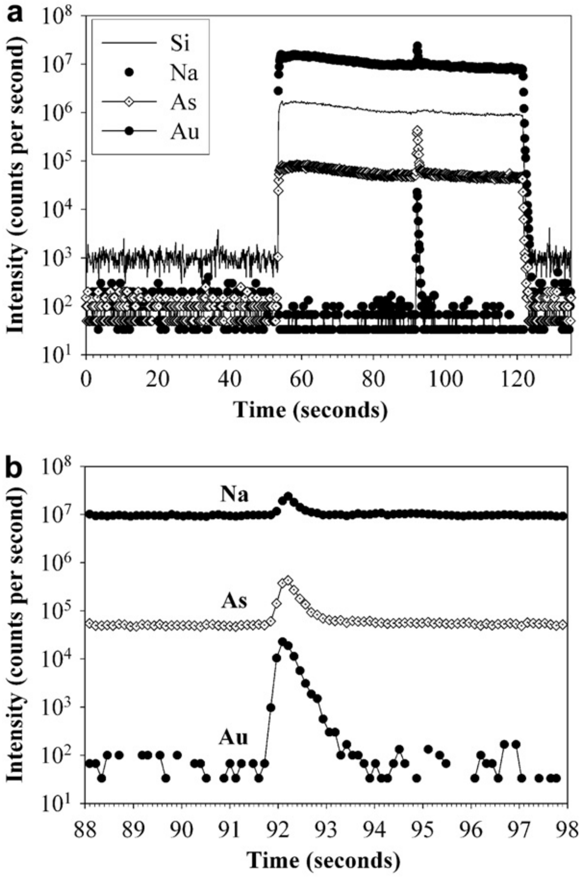

Fig. 4. (a) LA-ICPMS transient signal of a glass-hosted vapor fluid inclusion (~60 μm across; 1.8 wt% NaCl eq.; shot ma11a05). A 75 μm beam diameter was used to ablate the entire inclusion. Ablation of glass began at ~53 s and the fluid inclusion was liberated from ~92 to 94 s. Note that the glass volumes above and below the fluid inclusion are homogeneous with respect to As and Au. (b) The signal from Fig. 4a focusing only on the transient signal for the ablated fluid inclusion. The Au and As signals rise and fall with Na suggesting that that the Au and As are fully contained inside the fluid inclusion.

for As and the long tail stretching out to 86 s suggest that this Au signal results from the ablation of an accidentally trapped Au particle. The calculated Au concentration is 1092 μg/g if this Au signal is included in the data reduction. All other analyses of vapor inclusions from this run display Au signals which are clearly part of the fluid inclusion and yield an average Au concentration (±1σ) of 13 ± 2 μg/g (see Fig. 4). We suggest that the transient signal shown in Fig. 5a and b reflects the nucleation of a Au particle during quench and the contemporaneous nucleation and growth of a fluid inclusion on this Au particle. This explains the intimate physical association of the two phases in the glass. Fewer than 5% of the fluid inclusions displayed signals similar to that shown in Fig. 5. Such fluid inclusions which displayed anomalously large Au signals were not processed. We suggest that the As and Au concentrations for both S-free and S-bearing runs provide a reasonable estimate of As content and Au solubility in magmatic vapor at the P, T, f_{O_2}, f_{S_2}, f_{H_2S} run conditions.

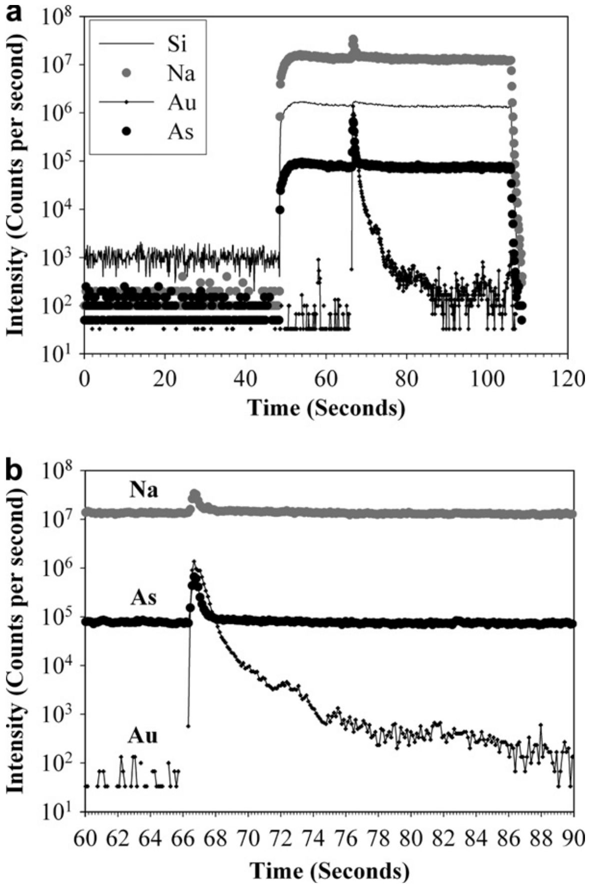

Fig. 5. (a) LA-ICPMS transient signal of a glass-hosted fluid inclusion (shot ma11a03). The fluid inclusion is noted by the increase in Na intensity between 64 and 68 s. The increase in Au intensity occurs at approximately the same time. However, the intensity of the Au signal is several orders of magnitude greater than in most other fluid inclusions ablated from the same glass volume. (b) The analysis ma11a03 focusing on the transient signal for the fluid inclusion. Note that Au intensity climbs parallel with As and Na; however, the anomalously high Au intensity relative to all other analyses of this glass and the long tail suggest that this signal records the presence of a Au particle which served as a nucleation site for the fluid inclusion. Shots displaying signals such as this one were ignored during data reduction as their inclusion would yield erroneously high Au solubility values for vapor and concomitantly low vapor/melt partition coefficients.

3.1.3. Arsenic and gold partitioning between vapor and melt

The metal concentrations presented in Table 3 were used to calculate Nernst-type partition coefficients for As and Au between vapor and melt defined by:

$$D_{\mathrm{As}}^{\mathrm{v/m}} = C_{\mathrm{As}}^{\mathrm{vapor}} / C_{\mathrm{As}}^{\mathrm{melt}} \qquad (6)$$

$$D_{\mathrm{Au}}^{\mathrm{v/m}} = C_{\mathrm{Au}}^{\mathrm{vapor}} / C_{\mathrm{Au}}^{\mathrm{melt}} \qquad (7)$$

where C_i^j represents the concentration of component i in phase j as reported in Table 3. Uncertainties were calculated using the general error propagation formula. The calculated partition coefficients, $D_i^{\mathrm{v/m}}$ (±1σ), are presented in Table 4. The partition coefficient for As in S-free runs ranges from 0.7 to 1.2 with a mean of 1.0 ± 0.1. The partition coefficient for Au in S-free runs ranges from 6 to 21 with an average

Table 4
Partition coefficients (±1σ) for As and Au between co-existing vapor and melt at 800 °C and 120 MPa

Run#	$D_{\mathrm{As}}^{\mathrm{v/m}}(\pm 1\sigma)$	$D_{\mathrm{Au}}^{\mathrm{v/m}}(\pm 1\sigma)$
S-free runs		
As-7	0.7 (0.3)	15 (5)
As-8	0.9 (0.4)	18 (6)
As-9	1.1 (0.4)	21 (6)
As-10	1.2 (0.5)	13 (5)
As-11	0.9 (0.5)	6 (1)
S-bearing runs		
As-19	1.4 (0.3)	19 (14)
As-21	2.6 (0.4)	25 (22)
As-22	2.7 (0.4)	32 (19)
As-23	2.4 (0.3)	50 (38)
As-25	3.5 (1.6)	12 (5.5)
As-26	2.7 (1.6)	11 (8)

value of 15 ± 2.5. The partition coefficient for As in S-bearing runs ranges from 1.4 to 3.5 with a mean of 2.5 ± 0.3. The partition coefficient for Au in S-bearing runs ranges from 11 to 50. As discussed below, the S-bearing experiments run for ~400 h or less (As-19, As-21, As-22, and As-23) yield calculated values for $D_{\mathrm{Au}}^{\mathrm{v/m}}$ which are 2–4 times higher than experiments run for 689 and 936 h (As-25 and As-26, respectively). The partition coefficient values calculated from the longer duration experiments provide the best estimate of equilibrium vapor/melt partitioning and, thus, we suggest the best value for $D_{\mathrm{Au}}^{\mathrm{v/m}}$ is 12 ± 0.3 based on runs As-25 and As-26.

4. DISCUSSION

4.1. Melt–vapor partitioning

4.1.1. Arsenic behavior in S-free and S-bearing systems

Fig. 6 shows values for $D_{\mathrm{As}}^{\mathrm{v/m}}$ plotted against run time for both the S-free and S-bearing assemblages. The values of $D_{\mathrm{As}}^{\mathrm{v/m}}$ are constant, within the uncertainty of the data set, over run durations ranging from 353 to 1192 h and 187 to 936 h in the S-free and S-bearing runs, respectively, and are interpreted to represent equilibrium partition coefficient values. Our data suggest that the melt/vapor partition coefficient increases upon the addition of S to the experiment. Elemental speciation calculations using SUPCRT92 (Johnson et al., 1992) indicate that As^{3+} is favored at the experimental conditions of this study (Dimitri Sverjensky, personal communication). Pokrovski et al. (2002a) report that arsenous acid is the dominant As-species in vapor which contains up to ~0.5 molal H_2S or HCl. They use their experimental data to model the behavior of As in magmatic gases at temperatures from 200 to 1000 °C and conclude that arsenous acid is the dominant As-complex (>99% of the total As). However, the S-bearing data in this study suggests that S increases the affinity of As for magmatic vapor. The concentration of H_2S in the S-bearing experiments described herein is on the order of 0.7 molal; the concentration of H_2S in the experiments described by Pokrovski et al. (2002b) is on the order of 0.5 molal. The increased mass transfer of As from melt to vapor in the present study may reflect the increased abundance of reduced S in the vapor phase.

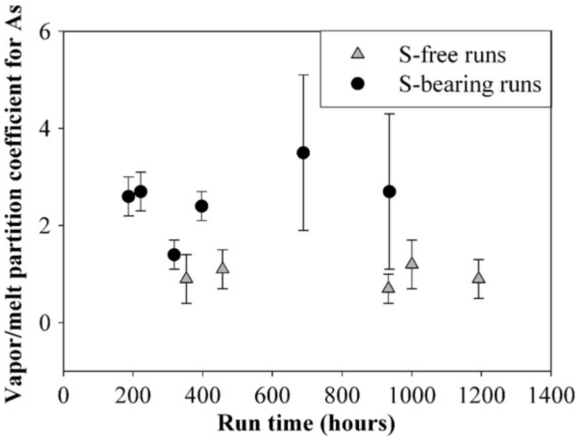

Fig. 6. The calculated Nernst-type partition coefficients for As in S-free and S-bearing melt–vapor experiments are plotted as a function of run duration. The data suggest that equilibrium was reached in both sets of experiments.

Arsenic is most likely present in silicate melts as As_2O_3 and the mass transfer of As from the melt to an aqueous phase most likely involves the hydrolysis of As_2O_3. Our partitioning data for As between high temperature rhyolite melt and low-salinity aqueous vapor suggest that As partitioning can be described by the equilibrium:

$$\frac{1}{2}\mathrm{As_2O_3^{melt}} + \frac{3}{2}\mathrm{H_2O} = \mathrm{As(OH)_3^{v}} \tag{8}$$

with the corresponding apparent equilibrium constant:

$$K'_{\mathrm{As}} = \frac{(C^{\mathrm{v}}_{\mathrm{As(OH)_3}})}{(C^{\mathrm{m}}_{\mathrm{As_2O_3}})^{1/2} * (X^{\mathrm{v}}_{\mathrm{H_2O}})^{3/2}} \tag{9}$$

where $C^{\mathrm{v}}_{\mathrm{As(OH)_3}}$ is the concentration of As in the vapor, $C^{\mathrm{m}}_{\mathrm{As_2O_3}}$ stands for the concentration of As in the melt and $X_{\mathrm{H_2O}}$ is the mole fraction of water in the vapor. Raoultian behavior was assumed for water (i.e., $a^{\mathrm{v}}_{\mathrm{H_2O}} = X^{\mathrm{v}}_{\mathrm{H_2O}}$) and $X_{\mathrm{H_2O}}$ was calculated by using mass balance; the vapor salinity on the order of 2 wt% NaCl eq. indicates that water dominates the mass of the vapor. Values for K'_{As} are tabulated in Table 5. The reported uncertainties for K'_{As} were determined by using the general error propagation formula: $K'_{\mathrm{As}} = (\mathrm{d}x/\mathrm{d}a)^2 * e_a^2 + (\mathrm{d}x/\mathrm{d}b)^2 * e_b^2 + \cdots (\mathrm{d}x/\mathrm{d}n)^2 * e_n^2$. The average value (±1σ) of $\log K'_{\mathrm{As}}$ is −1.3 (0.1) for the S-free runs and $\log K'_{\mathrm{As}}$ is −1.1 (0.1) for the S-bearing runs. The increase in the value of K'_{As} with the addition of sulfur may be attributed to the potential existence of an As–S complex in the vapor; however, this hypothesis awaits further experiments. Other factors may be responsible for the enhanced mass transfer of As into the vapor phase. The presence of high concentrations of H_2S increases both the salinity and acidity of the vapor phase and variations in these parameters may lead to higher concentrations of As in the vapor. Future experiments will be performed to elucidate As partitioning in more complex assemblages (i.e., vapor + brine + melt) and As-speciation in high-temperature vapor.

Table 5
Calculated values for the apparent equilibrium constants describing As and Au between melt and aqueous vapor

Run#	$\log K'_{\mathrm{As}}(\pm 1\sigma)$	$\log K'_{\mathrm{Au}}(\pm 1\sigma)$
S-free runs		
As-7	−1.4 (−1.8)	−4.2 (−4.8)
As-8	−1.3 (−2.1)	−4.4 (−4.9)
As-9	−1.1 (−1.7)	−4.4 (−5.1)
As-10	−1.2 (−1.7)	−4.3 (−4.7)
As-11	−1.3 (2.0)	−4.6 (−5.4)
S-bearing runs		
As-19	−1.2 (−1.9)	−3.2 (−3.4)
As-21	−1.0 (−1.7)	−3.8 (−4.0)
As-22	−1.1 (−1.8)	−4.1 (−4.3)
As-23	−1.1 (−1.8)	−3.9 (−4.1)
As-25	−1.1 (−1.8)	−4.3 (−4.7)
As-26	−0.9 (−1.4)	−4.1 (−4.3)

The geological significance of S on the mass transfer of As from silicate melt to low-salinity vapor can be assessed following Candela and Holland (1986). Their model allows the calculation of the efficiency with which vapor can scavenge As from melt as a function of the bulk partition coefficient $\overline{D}_{\mathrm{As}}$, the ratio of the initial water concentration ($C^{l,0}_{\mathrm{H_2O}}$) to the saturation water concentration ($C^{l,s}_{\mathrm{H_2O}}$), and the Nernst-type partition coefficient for As between vapor and melt $D^{\mathrm{v/m}}_{\mathrm{As}}$ for a silicate melt which degasses owing to crystallization (i.e., second boiling) using the equation

$$E(\mathrm{As}) = \left[\frac{C^{l.0}_{\mathrm{H_2O}}}{C^{l,s}_{\mathrm{H_2}O}}\right]^{\overline{D}_{\mathrm{As}}} \times \left[1 + \frac{\overline{D}_{\mathrm{As}}}{C^{l,s}_{\mathrm{H_2}O} \times D^{\mathrm{v/m}}_{\mathrm{As}}}\right]^{-1} \tag{10}$$

Eq. (10) assumes constant partition coefficients values; if the partition coefficients vary as a function of the concentration of Cl, HCl, H_2S, *inter alia* then the accuracy of the calculation is reduced. We do not have partitioning data for As between silicate melt and pyrrhotite and magnetite and, thus, data from natural assemblages were used to calculate the value of $\overline{D}_{\mathrm{As}}$. Stimac and Hickmott (1994) report that $D^{\mathrm{po/m}}_{\mathrm{As}}$ is on the order of 3; this value is based on the analyses of separated pyrrhotite phenocrysts and rhyolite. Ewart and Griffin (1994) report values for $D^{\mathrm{mt/m}}_{\mathrm{As}}$ ranging from 1.1 for magnetite and low-silicate rhyolite to 3.6 for magnetite and quartz latite. Assuming permissible mass fraction ranges for both pyrrhotite (0.025–0.01%) and magnetite (0.017–8.6%) in natural silicate melts yields values for $\overline{D}_{\mathrm{As}}$ on the order of 0.02 and 0.09 for assemblages with low and high modal abundances of magnetite and pyrrhotite, respectively; that is As behaves near perfectly incompatibly during crystallization. Assuming that $D^{\mathrm{v/m}}_{\mathrm{As}}$ values of 1.0 and 2.5 in the S-free and S-bearing assemblages remain constant during crystallization, Eq. (10) indicates that 41% and 62% of the As in the water-saturated melt may be scavenged by a S-free and S-bearing low-salinity vapor at low modal abundances of magnetite and pyrrhotite, respectively. If the modal abundance of pyrrhotite and magnetite is higher, yet still reasonable values, then S-free and S-bearing low-salinity vapor could scavenge 78% and 89% of the As contained in the water-saturated melt. These model calculations suggest that the ability of low-salinity vapor to scavenge and transport As from a crystallizing silicate melt is affected moderately by the quantity of pyrrhotite and magnetite in the fractionating assemblage. For a 1 km^3 S-free silicate melt with an initial concentration of As on the order of 1 μg/g (Gao et al., 1998) and an efficiency of As removal of 78% (S-free system), this implies that a S-free low-salinity vapor may scavenge on the order of 2.1×10^3 kg of As from the melt. The addition of S to the same 1 km^3 silicate melt results in the scavenging of 2.4×10^3 kg of As from the melt at an efficiency of removal of 89%. Thus, the increase in the value of $D^{\mathrm{v/m}}_{\mathrm{As}}$ from 1 in the S-free assemblage to 2.6 in the S-bearing assemblage results in the mass transfer of an additional 300 kg of As from the melt to the vapor. The model calculations demonstrate that moderate changes in $D^{\mathrm{v/m}}_{\mathrm{As}}$ have a relatively small effect on the As budget of an evolving rhyolite magma.

4.1.2. Gold behavior in S-free and S-bearing systems

The S-free glass data presented here are consistent with Au solubility values reported in other studies. Frank et al. (2002) report that Au solubility in S-free rhyolite glass equilibrated with S-free brine is on the order of 1 μg/g at 800 °C, 100 MPa and $f_{\mathrm{O_2}} = \mathrm{NNO}$. Simon et al. (2005) report that Au solubility in S-free rhyolite glass remains constant at ~0.5 μg/g at 800 °C, 100–145 MPa and $f_{\mathrm{O_2}} = \mathrm{NNO}$ in a S-free rhyolite melt–vapor–brine–magnetite assemblage. Thus, the value of 2.5 ± 0.7 μg/g reported here for S-free glass is elevated slightly albeit consistent with extant data.

The reported value for Au solubility of 0.60 ± 0.16 μg/g in the S-bearing glasses is lower, albeit consistent with extant data for a rhyolite melt–sulfide–vapor assemblage at magmatic conditions. Jugo et al. (1999) report that Au solubility in rhyolite glass equilibrated with pyrrhotite and intermediate solid solution and vapor is 4.1 ± 2.4 μg/g at 850 °C, 100 MPa, $f_{\mathrm{O_2}} = \mathrm{NNO} - 0.25$ and $\log f_{\mathrm{S_2}} = -1.0 \pm 0.7$; they calculated $f_{\mathrm{S_2}}$ following the method outlined Toulmin and Barton (1964). The experiments performed by Jugo et al. (1999) contained higher HCl concentrations in both melt and vapor and, thus, their reported higher Au solubility values in melt may reflect the increased acidity of their assemblage. The new Au solubility data and those reported by Jugo et al. (1999) indicate that the solubility of Au varies between about 0.5 and 4 μg/g. This variation is most likely a function of changes in HCl concentration and $f_{\mathrm{S_2}}$ between the experimental studies and is the subject of a separate paper currently in progress.

The partitioning of Au between vapor and melt is shown as a function of run time in Fig. 7. The data for the S-free assemblage fall along an array with a slope nearly parallel to the abscissa indicating no statistically relevant change in the partition coefficient with run times approaching 1200 h. The lack of variation in $D^{\mathrm{v/m}}_{\mathrm{Au}}$ suggests that the S-free melts reached equilibrium with respect to Au within ~400 h. This timeframe also accords with the calculated time for Au to diffuse throughout the melt volume as discussed above. The S-free partitioning data are consistent with data reported in Simon et al. (2005). They constrained quantitatively the partitioning of Au between Au-saturated

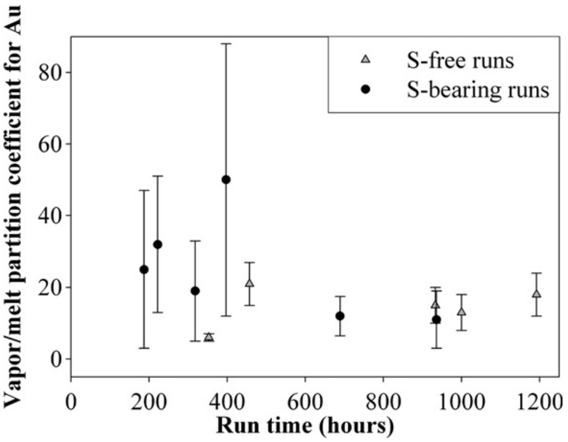

Fig. 7. The calculated Nernst-type partition coefficients for Au in S-free and S-bearing melt–vapor experiments are plotted as a function of run duration. The higher vapor/melt partition coefficients for the S-bearing runs of less than ~400 h may reflect disequilibrium and, thus, only the partition coefficients for the longer duration runs were used in calculations presented in the text. The vapor/melt partition coefficients calculated from the S-free data suggest that equilibrium was reached in all experiments.

haplogranite and low-salinity vapor in a melt–vapor–brine–magnetite system at 800 °C and pressures of 110, 130, 140, and 145 MPa. Simon et al. (2005) report values (±1σ) for $D_{\mathrm{Au}}^{\mathrm{v/m}}$ of 10 ± 2, 8 ± 2, 56 ± 16, and 72 ± 15 at 110, 130, 140, and 145 MPa, respectively. The mean value of 15 ± 2.5 reported here is consistent with Simon et al. (2005) and indicates that the mass transfer of Au from melt to vapor is essentially constant between 110 and 130 MPa, but increases at higher pressures owing to the higher concentration of HCl present in the vapor phase if the bulk salinity of the vapor is constrained to lie just outside the brine-undersaturated vapor limb of the solvus. The partitioning data derived from the S-bearing experiments exhibit more scatter relative to the S-free data. The values of $D_{\mathrm{Au}}^{\mathrm{v/m}}$ range from 19 to 50 over run times from ~200 to ~ 400 h. Increasing the run time to 689 and 936 h results in $D_{\mathrm{Au}}^{\mathrm{v/m}}$ values of 12 and 11, respectively. We suggest that the values for$D_{\mathrm{Au}}^{\mathrm{v/m}}$ calculated from the longer duration runs provide the best estimate for vapor/melt partitioning (cf. Tacker and Candela, 1987). These data yield an average value for $D_{\mathrm{Au}}^{\mathrm{v/m}}$ of 12 ± 0.3 for the S-bearing assemblage.

The calculated value for $D_{\mathrm{Au}}^{\mathrm{v/m}}$ in both the S-free and S-bearing assemblages are lower by one order of magnitude than the value of $D_{\mathrm{Au}}^{\mathrm{v/m}} = 300 \pm 175(1\sigma)$ reported by Candela et al. (1996). They quantified experimentally the partitioning of Au in a rhyolite melt–supercritical volatile phase–pyrrhotite–Au metal assemblage at 140 MPa and 800 °C. The solubility of Au in the H_2O-saturated rhyolite in their study was on the order of 2–4 μg/g and the solubility of Au was several hundreds of μg/g in the low-sulfur supercritical volatile phase. The higher calculated $D_{\mathrm{Au}}^{\mathrm{v/m}}$ reported by Candela et al. (1996) may have resulted from the increased total salinity (3 wt% NaCl eq.) and HCl concentration of the volatile phase in their experiments. Candela et al. (1996) concluded that reduced, sulfur-bearing conditions are not a fundamental requirement for the efficient mass transfer of Au from the melt to a volatile phase. The new results presented here, coupled with the S-free data reported by Simon et al. (2005), support their conclusion.

The partitioning of gold between silicate melt and an aqueous volatile phase(s) is controlled dominantly by pressure, temperature, and the acidity of the aqueous phase. The partition coefficients reported here are valid only for the experimental conditions noted in this study. Changes in temperature, pressure, gas fugacities, changes in the vapor chemistry and the concentration of HCl in the aqueous phase, changes in melt composition, *inter alia* will cause the partition coefficient to vary. As such, apparent equilibrium constants were calculated to thermodynamically describe and compare the partitioning behavior of Au in S-free and S-bearing magmatic assemblages. The partitioning of Au between melt and vapor can be described by the apparent equilibrium constant:

$$K'_{\mathrm{Au}} = \frac{C_{\mathrm{Au}}^{\mathrm{v}} * (f_{\mathrm{H_2O}})^{0.5}}{C_{\mathrm{Au}}^{\mathrm{m}} * (C_{\mathrm{HCl}}^{\mathrm{v}})^{2}} \tag{11}$$

where $C_{\mathrm{Au}}^{\mathrm{v}}$ is the concentration of Au in the vapor phase, $C_{\mathrm{Au}}^{\mathrm{m}}$ is the concentration of Au in the silicate glass, $C_{\mathrm{HCl}}^{\mathrm{v}}$ is the concentration of HCl in the vapor and $f_{\mathrm{H_2O}}$ is the fugacity of water at P and T. Values of K'_{Au}, provided in Table 5, were calculated by using the S-free and S-bearing data in Table 3. The average value of log K'_{Au} (±1σ) is −4.4 (0.1) in the S-free system. Data for the S-bearing system, using only the long duration experiments, yield a mean value of log K'_{Au} (±1σ) equal to −4.2 (0.2). The overlapping values for K'_{Au} the S-free and S-bearing experiments suggest that the overall effect of S on the mass transfer of Au from rhyolite melt to a low-salinity vapor, at the experimental conditions described herein, is insignificant with respect to the Au-ore potential of a low-$f_{\mathrm{S_2}}$ rhyolite which is degassing a low-salinity vapor. The calculated efficiencies of removal (presented below) illustrate this.

The geologic significance of the effect of S on the mass transfer of Au from a degassing silicate melt to an exsolved low-salinity vapor can be evaluated following Candela and Holland (1986) as discussed previously for As (see Eq. (10)). The value for $\overline{D}_{\mathrm{Au}}$ was calculated by using values for $D_{\mathrm{Au}}^{\mathrm{mt/m}}$ and $D_{\mathrm{Au}}^{\mathrm{po/m}}$ of 4 (Simon et al., 2003) and 140 (Jugo et al., 1999), respectively. The calculated efficiencies of Au removal from a water-saturated melt are 93% and 91% in the S-free and S-bearing assemblages at low modal abundances of magnetite (1.7) and pyrrhotite (0.025%), respectively. Assuming a Au concentration on the order of 1 μg/g (1×10^{-12} kg/kg) in a rhyolite melt, the calculated efficiencies of removal (Eq. (10)) indicate that S-free and S-bearing vapor can scavenge on the order of 5.0×10^{3} kg Au and 4.9×10^{3} kg of Au from a 1 km^3 melt which contains low modal abundances of both magnetite and pyrrhotite. For a melt with high modal abundances of magnetite (8.6%) and pyrrhotite (0.1%), the efficiencies of removal are 72% and 60% for the S-free and S-bearing systems, respectively. The calculated efficiencies of removal (Eqn. (10)) indicate that S-free and S-bearing vapor can scavenge on the order of 3.9×10^{3} kg and 3.2×10^{3} kg of Au from a 1 km^3 melt which contains high modal abundances of both magnetite and pyrrhotite. Extending these calculations to the several 10–100 s of km^3 of magma that may underlie giant to super-giant porphyry deposits (Richards, 2005) indicates that low-salinity vapor may be responsible for delivering significant quantities of Au to the porphyry environment. For example, a low salinity vapor (~2 wt% NaCl eq.), with or without the presence of S, may scavenge on the order of 2.6×10^6 kg of Au from a 100 km^3 melt from which low modal abundances of both pyrrhotite and magnetite have crystallized. These model calculations demonstrate that the presence of S in low f_{S_2} magmatic vapor is not a prerequisite for the formation of a large tonnage Au-ore body. The direct effect of f_{S_2} on crystal/melt partitioning remains to be determined.

The presence of high concentrations of Au in natural vapor fluid inclusions (Ulrich et al., 1999; Williams-Jones and Heinrich, 2005) and the high mass ratio of vapor to brine in many magmatic-hydrothermal systems (Candela and Piccoli, 1995; Williams-Jones and Heinrich, 2005) coupled with the new data presented here suggest that magmatic vapor can be a highly effective agent of Au-ore deposition in magmatic-hydrothermal systems. Williams-Jones and Heinrich (2005) compiled chemical data from volcanic gases as well as vapor and brine fluid inclusions from multiple porphyry-type ore deposits and argue convincingly that vapor may be the dominant ore-transporting fluid in terms of the total mass of H_2O and potentially Cl and metals such as Au. To put this in perspective, consider that the total Au content of the Bajo de la Alumbrera deposit, Argentina, is on the order of 4.6×10^4 kg Au (Wall, 1997; Ulrich et al., 1999). If only low salinity vapor were responsible for Au deposition at Bajo de la Alumbrera, this would require a volume of magma on the order of 150 km^3. Sasso and Clark (1998) used field and aeromagnetic data to suggest that a pluton on the order 150 km^3 exists beneath Bajo de la Alumbrera. Geophysical evidence from numerous volcanic centers (e.g., Cascades, Kamchatka, Mt. Etna) also suggest the existence of magma bodies with sizes potentially up to 10^3–10^6 km^3 (Iyer, 1984). However, we note that the magma itself is a partial melt (i.e., melt + crystals) and, thus, the total volume of melt contained within the magma body will be much less than the total volume of magma. For example, the melt volume in the magma chamber residing beneath Yellowstone is estimated to occupy ~10% of the total volume of the magma body (R.L. Christiansen, personal communication). The inferred plutonic complex beneath Bajo de la Alumbrera probably represents the consolidation of multiple magma (i.e., melt ± crystals ± volatiles) batches. Therefore, Au and other metals may be derived from a time-integrated flux of dominantly low-salinity vapor exsolved from a series of sequential magma batches, rather than from a single magma chamber. While the efficiency calculations presented above suggest that low-salinity vapor could have transported enough Au to form the Au ore at Bajo de la Alumbrera, we point out that Ulrich et al. (1999) report that vapor fluid inclusions associated intimately with ore mineralization contain no greater than 0.5 μg/g Au whereas co-existing brine inclusions contain 0.79 ± 0.39 μg/g Au. Ulrich et al. (1999) cite the overlapping Au/Cu ratios of brine fluid inclusions with the bulk Au/Cu ratio of the ore deposit as evidence that brine was the dominant ore–metal transporting agent at Bajo de la Alumbrera. The low Au concentrations in vapor may lead one to assume that vapor was unimportant in the development of the Au ore; however, this may not be the case considering that the mass fraction of vapor may have exceeded significantly that of brine. Ulrich et al. (1999) also report Au concentrations in vapor (10.17 ± 6.20 μg/g) and brine (0.26 ± 0.18 μg/g) fluid inclusions from the Au porphyry at Grasberg, the world's largest Au deposit containing an estimated 1.5×10^6 kg Au. Homogenization temperatures for vapor and brine inclusions approach ~700 °C suggesting that the fluid inclusions may preserve near-magmatic compositions. The Au/Cu ratios in brine inclusions from Grasberg also statistically overlap the Au/Cu ratio of the ore body; however, the Au/Cu ratio of the vapor inclusions at Grasberg are, on average, elevated relative to the bulk ore and the average concentration of Au in vapor is forty times higher than in the brine. The high Au concentrations in the Grasberg vapor inclusions may reflect higher concentrations of Au-complexing ligands such as HCl (Williams et al., 1995, 1997), OH (Gammons and Williams-Jones, 1997) and or HS (Heinrich et al., 1999; Simon et al., 2006) in the vapor. These data suggest that vapor could have transported a significant quantity of Au in the Grasberg system. We do not mean to suggest that magmatic-hydrothermal brine is unimportant in transporting Au. Rather, our data presented here coupled with the high Au concentrations in natural vapor inclusions (Heinrich et al., 1999; Ulrich et al., 1999) suggest that low-salinity vapor may be a much more efficient and important Au-transporting agent than previously believed.

5. CONCLUDING REMARKS

The data presented here suggest that As is transported as arsenous acid in S-free low-salinity magmatic vapor, in agreement with previous studies (Pokrovski et al., 2002a). However, the addition of S to the magmatic assemblage increases the mass transfer of As from melt to vapor by a factor of 2.5 and suggests the potential existence of an As–S species in the vapor phase. The increased partitioning results in a greater quantity of As being scavenged and advected from a silicate melt during degassing.

The presence of S does not increase the partitioning of Au from silicate melt to a low-salinity vapor at 800 °C, 120 MPa, $f_{O_2} = \text{NNO}$, $\log f_{H_2S} = 1.1$, $\log f_{SO_2} = -1.5$, and $\log f_{S_2} = -3.0$. Efficiency of removal calculations demonstrate that S affects minimally the ability of a low-salinity magmatic vapor to scavenge Au from a rhyolite melt at the aforementioned conditions. These results suggest that Au-speciation in S-bearing, low-salinity magmatic vapor at the experimental conditions given above is dominated by gold(I)chloride, in agreement with previous studies (Frank et al., 2002; Stefánsson and Seward, 2003, 2004; Simon et al., 2005). This study did not address the potential effects of gold(I) hydroxyl complexation which may be significant under select physicochemical conditions (Gammons and Williams-Jones, 1997; Frank et al., 2002).

These findings have implications for the hypothesis that gold(I)-bisulfide may exist in magmatic-hydrothermal vapor (Audétat et al., 1998; Heinrich et al., 1999). The new data demonstrate that at low values of f_{S_2} (i.e., $\log f_{S_2} = -3$), and high ratios of reduced to oxidized sulfur (i.e., $H_2S:SO_2 = 400$), the presence of H_2S does not increase the Au-scavenging potential of low-salinity aqueous vapor at magmatic conditions. Future experiments are planned to constrain the speciation of Au in magmatic volatile phases across a range of P, T, f_{O_2}, f_{S_2}, pH conditions and the effect of f_{S_2} on crystal/melt equilibria.

ACKNOWLEDGMENTS

This work was partially supported by National Science Foundation Grants: EAR 0309967 (P.A.C. and P.M.P.), EAR 9909576 (P.A.C. and P.M.P.) and EAR 0125805 (P.A.C. and P.M.P.); EAR 9810244 (P.M.P. and others). We thank Steve Kesler, John Mavrogenes and Anthony Williams-Jones for their thorough and constructive reviews which strengthened the substance and conclusions of the paper. Associate Editor Ed Ripley is thanked for his expediency in handling the manuscript. The Isotope Geochemistry and Mineral Resources group at ETH acknowledges continued support from the Swiss National Science Foundation. A.C.S. thanks his family for their support.

REFERENCES

Acosta-Vigil A., London D., Morgan G. B., and Dewers, VI, T. A. (2003) Solubility of excess alumina in hydrous granitic melts in equilibrium with peraluminous minerals at 700–800 °C and 200 MPa, and applications of the aluminum saturation index. *Contrib. Miner. Petr.* **146**, 100–119.

Anderko A., and Pitzer K. S. (1993) Equation-of-state representation of phase equilibria and volumetric properties of the system NaCl–H_2O above 573 K. *Geochim. Cosmochim. Acta* **57**, 1657–1680.

Arribas A., Hedenquist J. W., Itaya T., Okada T., Concepción R. A., and Garcia, Jr., J. S. (1995) Contemporaneous formation of adjacent porphyry and epithermal Cu–Au deposits over 300,000 years in northern Luzon, Philippines. *Geology* **23**, 337–340.

Audétat A., Günther D., and Heinrich C. A. (1998) Formation of a magmatic hydrothermal ore deposit; insights in with LA-ICP-MS analysis of fluid inclusions. *Science* **279**, 2091–2094.

Audétat A., Günther D., and Heinrich C. A. (2000) Causes for large-scale metal zonation around mineralized plutons: fluid inclusion LA-ICP-MS evidence from the Mole Granite, Australia. *Econ. Geol.* **95**, 1563–1581.

Audétat A., and Pettke T. (2003) The magmatic-hydrothermal evolution of two barren granites: a melt and fluid inclusion study of the Rito del Medio and Cañada Pinabete plutons in northern New Mexico (USA). *Geochim. Cosmochim. Acta* **67**, 97–121.

Bailey D. K., Cooper J. P., and Knight J. L. (1974) Anhydrous melting and crystallization of peralkaline obsidians. *Bull. Volcanol.* **38**, 653–665.

Bailey D.K., and Cooper J. P. (1978) Comparison of the crystallization of pantelleritic obsidian under hydrous and anhydrous conditions. In *Progress in Experimental Petrology; Fourth Progress Report of Research Supported by N.E.R.C.* (ed. W. S. MacKenzie) 1975–1978, pp. 230–233.

Baker L., and Rutherford M. J. (1996) Crystallisation of anhydrite-bearing magmas. *Proc. R. Soc. Edinb. Earth Sci.* **87**, 243–250.

Ballantyne J. M., and Moore J. N. (1988) Arsenic geochemistry in geothermal systems. *Geochim. Cosmochim. Acta* **52**, 473–483.

Barnes H. L., and Seward T. M. (1997) Geothermal systems and mercury deposits. In *Geochemistry of Hydrothermal Ore Deposits* (ed. H.L. Barnes), 3rd ed. John Wiley, New York, pp. 699–736.

Barton P. B. (1969) Sulfide petrology. *Miner. Soc. Am. Spec. Paper* **3**, 187–198.

Belonoshko A. B., Shi P. F., and Saxena S. K. (1992) A FORTRAN-77 program for calculation of Gibbs free energy and volume of C–H–O–S–N–Ar mixtures. *Comput. Geosci.* **18**, 1267–1269.

Berger B. R. (1985) Geologic-geochemical features of hot-spring precious metal deposits. *U.S. Geol. Surv. Bull.* **1646**, 47–53.

Berger B. R. (1986) Descriptive model of hot-spring Au–Ag. In *Mineral Deposit Models* (eds. D. P. Cox and D. A. Singer). U.S. Geological Survey Bulletin, 1693, p. 143.

Bodnar R. J., and Vityk M. O. (1994) Interpretation of microthermometric data for H_2O NaCl fluid inclusions. In *Fluid Inclusions in Minerals, Methods and Applications* (eds. B. De Vivo and M.L. Frezzotti). Virginia Polytechnic Institute, VA, pp. 117–130.

Bodnar R. J., Burnham C. W., and Sterner S. M. (1985) Synthetic fluid inclusions in natural quartz. III. Determination of phase equilibrium properties in the system H_2O–NaCl to 1000 °C and 1500 bars. *Geochim. Cosmochim. Acta* **49**, 1861–1873.

Burnham C. W. (1979). Magmas and hydrothermal fluids. In *Geochemistry of Hydrothermal Ore Deposits* (ed. H.L. Barnes). Wiley, New York, pp. 71–136.

Cameron E. M., Leybourne M. I., and Kelley D. L. (2002) Exploring for deeply covered mineral deposits: Formation of geochemical anomalies in northern Chile by earthquake-induced surface flooding of mineralized groundwaters. *Geology* **30**(11), 1007–1010.

Candela P. A., and Holland H. D. (1984) The partitioning of copper and molybdenum between melts and aqueous fluids. *Geochim. Cosmochim. Acta* **48**, 373–380.

Candela P. A., and Holland H. D. (1986) A mass transfer model for copper and molybdenum in magmatic hydrothermal systems; the origin of porphyry-type ore deposits. *Econ. Geol.* **81**, 1–19.

Candela P. A., and Piccoli P. M. (1995) Model ore–metal partitioning from melts into vapor and vapor/brine mixtures. In *Magmas, Fluids, and Ore Deposits*, vol. 23 (ed. J. F. H. Thompson). Mineralogical Association of Canada Short Course, pp. 101–128.

Candela P. A., Piccoli P. M., and Williams T. J. (1996) Preliminary study of gold partitioning in a low sulfur, high oxygen fugacity melt/volatile phase system. GSA Abstracts with Programs.

Candela P. A., and Piccoli P. M. (2005) Magmatic processes in the development of porphyry-type ore systems. In *Econ. Geol. 100th Anniv. Vol.* (eds. J. W. Hedenquist, J. F. H. Thompson, R. J. Goldfarb, and J. P. Richards), pp. 25–38.

Carmichael I. S. E., and MacKenzie W. S. (1963) Feldspar-liquid equilibria in pantellerites: an experimental study. *Am. J. Sci.* **261**, 382–396.

Charles R. W., and Vidale R. (1982) Temperature calibration of a new rapid quench vessel. *Am. Miner.* **67**, 175–179.

Chou I. C. (1987) Oxygen buffer hydrogen sensor techniques at elevated pressures and temperatures. In *Hydrothermal Experimental Techniques* (eds. G. C. Ulmer and H. L. Barnes), pp. 61–99.

Chou I. C. (1987b) Phase relations in the system NaCl–KCl–H_2O: III, Solubilities of halite in vapor-saturated liquids above 445 degrees C and redetermination of phase equilibrium properties in the system NaCl–H_2O to 1000 degrees C and 1500 bars. *Geochim. Cosmochim. Acta* **51**, 1965–1975.

Chou I.-M., Sterner S. M., and Pitzer K. S. (1992) Phase relations in the system NaCl–KCl–H_2O: IV. Differential thermal analysis of the sylvite liquidus in the KCl–H_2O binary, the liquidus in the NaCl–KCl–H_2O ternary, and the solidus in the NaCl–KCl binary to 2 kb pressure, and a summary of experimental data for thermodynamic-PTX analysis of solid–liquid equilibria at elevated P–T conditions. *Geochim. Cosmochim. Acta* **56**, 2281–2293.

Clark L. A. (1960) The Fe–As–S system: phase relations and applications. *Econ. Geol.* **55**, Part I: 1345–1381, Part II: 1631–1652.

Clemente B., Scaillet B., and Pichavant M. (2004) The solubility of sulphur in hydrous rhyolitic melts. *J. Petrol.* **45**(11), 2171–2196.

Cline J., Hofstra A., Tosdal R. M., Muntean J., and Hickey, K. A. (2005) Carlin-type gold deposits in Nevada: critical geologic characteristics and viable model. In *Econ. Geol. 100th Anniv. Vol.* (eds. J. W. Hedenquist, J. F. H. Thompson, R. J. Goldfarb, and J. P. Richards), pp. 451–484.

Cooke D. R., and Simmons S. F. (2000) Characteristics and genesis of epithermal gold deposits. *Rev. Econ. Geol.* **13**, 221–244.

Cunneen R., and Sillitoe R. H. (1989) Paleozoic hot spring sinter in the Drummond Basin, Queensland, Australia. *Econ. Geol.* **84**, 135–142.

Dilles J. H. (1987) Petrology of the Yerington Batholith, Nevada; evidence for evolution of porphyry copper ore fluids. *Econ. Geol.* **82**, 1750–1789.

Dingwell D. B. (1998) Magma degassing and fragmentation. Recent experimental advances. In *Explosive Volcanism: A Physical Description* (eds. A. Freundt and M. Rosi), p. 318. Springer-Verlag.

Dingwell D. B. (2003) Liquid to glass: Quantifying properties and structure of melts across the glass transition. In *Melt Inclusions in Volcanic Systems* (eds. B. De Vivo and R.J. Bodnar). Elsevier, pp. 45–63.

Drummond S. E., and Ohmoto H. (1985) Chemical evolution and mineral deposition in boiling hydrothermal systems. *E.con. Geol.* **80**, 126–147.

Emmons W. H. (1927) Relations of disseminated copper ores in porphyry to igneous intrusions. *Am. Inst. Mining and Metall. Eng. Trans.* **75**, 797–809.

Ewart A., and Griffin W. L. (1994) Application of proton-microprobe data to trace-element partitioning in volcanic-rocks. *Chem. Geol.* **117**, 251–284.

Fleet M. E., Chryssoulis S. L., MacLean P. J., Davidson R., and Weisener C. G. (1993) Arsenian pyrite from gold deposits: Au and As distribution investigated by SIMS and EMPA, and color staining and surface oxidation by XPS and LIMS. *Can. Miner.* **31**, 1–17.

Frank M. R., Candela P. A., Piccoli P. M., and Glascock M. D. (2002) Gold solubility, speciation, and partitioning as a function of HCl in the brine-silicate melt-metallic gold system at 800 °C and 100 MPa. *Geochim. Cosmochim. Acta* **66**, 3719–3732.

Fulignati P., and Sbrana A. (1998) Presence of native gold and tellurium in the active high sulfidation hydrothermal system of the La Fossa volcano (Vulcano, Italy). *J. Volcanol. Geotherm. Res.* **86**, 187–198.

Gaillard F., Scaillet B., Pichavant M., and Beny J. M. (2001) The effect of water and fO_2 on the ferric–ferrous ratio of silicic melts. *Chem. Geol.* **174**, 255–273.

Gammons C. H., and Williams-Jones A. E. (1997) Chemical mobility of gold in the porphyry epithermal environment. *Econ. Geol.* **92**, 45–59.

Gao S., Luo T.-C., Zhang B.-R., Zhang H.-F., Han Y.-W., Zhao Z.-D., and Hu Y.-K. (1998) Chemical composition of the continental crust as revealed by studies in East China. *Geochim. Cosmochim. Acta* **62**, 1959–1975.

Günther D., Frischknecht R., Heinrich C. A., and Kahlert H. J. (1997) Capabilities of an Argon fluoride 193 nm Excimer laser ablation inductively coupled plasma mass spectrometry microanalysis of geological materials. *J. Anal. Atomic Spec.* **12**, 939–944.

Günther D., Audétat A., Frischknecht A., and Heinrich C. A. (1998) Quantitative analysis of major, minor, and trace elements in fluid inclusions using laser ablation-inductively coupled plasma mass spectrometry. *J. Anal. Atom. Spec.* **13**, 263–270.

Halter W. E., Heinrich C. A., and Pettke T. (2005) Magma evolution and the formation of porphyry Cu–Au ore fluids: evidence from silicate and sulfide melt inclusions. *Min. Deposita* **39**, 845–863.

Hanley J. J., Pettke T., Mungall J. E., and Spooner E. T. C. (2005) The solubility of platinum and gold in NaCl brines at 1.5 kbar, 600 to 800C: a laser ablation ICP-MS pilot study of synthetic fluid inclusions. *Geochim. Cosmochim. Acta* **69**, 2593–2611.

Hedenquist J. W. (1991) Boiling and dilution in the shallow portion of the Waiotapu geothermal system, New Zealand. *Geochim. Cosmochim. Acta* **55**, 2753–2765.

Hedenquist J. W., and Lowenstern J. B. (1994) The role of magmas in the formation of hydrothermal ore deposits. *Nature* **370**, 519–527.

Hedenquist J. W. (1995) The ascent of magmatic fluid: discharge versus mineralization. Mineralogical Association of Canada. *Short Course* **23**, 263–289.

Hedenquist J. W., Simmons S. F., Giggenbach W. F., and Eldridge C. S. (1993) White Island volcanic hydrothermal system as an active analogue of the environment of high sulfidation Cu and Au ore deposition. *Geology* **21**, 731–734.

Hedenquist J. W., Aoki M., and Shinohara H. (1994) Flux of volatile and ore-forming metals from the magmatic-hydrothermal system of Satsuma Iwojima volcano. *Geology* **22**, 585–588.

Hedenquist J. W., Arribas, Jr., A., and Reynolds T. J. (1998) Evolution of an intrusion centered hydrothermal system; Far Southeast-Lepanto porphyry and epithermal Cu–Au deposits, Philippines. *Econ. Geol.* **93**, 373–404.

Heinrich C. A., Ryan C. G., Mernagh T. P., and Eadington P. J. (1992) Segregation of ore metals between magmatic brine and vapor: a fluid inclusion study using PIXE microanalysis. *Econ. Geol.* **87**, 1566–1583.

Heinrich C. A., Günther D., Audétat A., Ulrich T., and Frischknecht R. (1999) Metal fractionation between magmatic brine and vapor, determined by microanalysis of fluid inclusions. *Geology* **27**, 755–758.

Heinrich C. A., Pettke T., Halter W. E., Aigner-Torres M., Audétat D., Günther D., Hattendorf D., Bleiner D., Guillong M., and Horn I. (2003) Quantitative multi-element analysis of minerals, fluid and melt inclusions by laser-ablation inductively-coupled plasma mass spectrometry. *Geochim. Cosmochim. Acta* **67**, 3473–3497.

Hofstra A. H., and Cline J. S. (2000) Characteristics and models for Carlin-type gold deposits. In *SEG Reviews in Economic Geology Gold 2000*, vol. 13 (eds. S. G. Hagemann and P. E. Brown), pp. 163–220.

Holland H. D. (1972) Granites, solutions, and base metal deposits. *Econ. Geol.* **67**, 281–301.

Holloway J. R. (1977) Fugacity and activity of molecular species in supercritical fluids. In *Thermodynamics in Geology* (ed. D.G. Fraser). Reidel, Dordrecht, The Netherlands, pp. 161–181.

Huebner J. S., and Sato M. S. (1970) The oxygen fugacity–temperature relationships of manganese oxide and nickel oxide buffers. *Am. Miner.* **55**, 934–938.

Iyer H. M. (1984) A review of crust and upper mantle structure studies of the Snake-RiverPlain-Yellowstone volcanic system: a major lithospheric anomaly in the western USA. *Tectonophysics* **105**, 291–308.

Johnson J. W., Oelkers E. H., and Helgeson H. C. (1992) SUPCRT92: A software package for calculating the standard molal thermodynamic properties of minerals, gases, aqueous species, and reactions from 1 to 5000 bar. *Comp. Geosci.* **18**, 899–947.

Jugo P. J., Candela P. A., and Piccoli P. M. (1999) Magmatic sulfides and Au:Cu ratios in porphyry deposits: an experimental study of copper and gold partitioning at 850 °C, 100 MPa in a haplogranitic melt–pyrrhotite–intermediate solid solution–gold metal assemblage, at gas saturation. *Lithos* **46**, 573–589.

Mambo V. S., Yoshida M., and Matsuo S. (1991) Partition of arsenic and phosphorous between volcanic gases and rock. Part I: analytical results and magmatic conditions of Mt. Usu, Japan. *J. Volcanol. Geotherm. Res.* **46**, 37–47.

Mambo V. S., and Yoshida M. (1993) Behavior of arsenic in volcanic gases. *Geochemical Journal* **27**, 315–359.

Marschik R., and Fontbote L. (2001) The Candelaria-Punta del Cobre Iron Oxide Cu–Au(–Zn–Ag) deposits, Chile. *Econ. Geol.* **96**, 1799–1826.

Morgan, VI, G. B., and London D. (1996) Optimizing the electron microprobe analysis of hydrous alkali aluminosilicate glasses. *Am. Miner.* **81**, 1176–1185.

Mustard R., Ulrich T., Kamanestky V. S., and Mernagh T. (2006) Gold and metal enrichment in natural granitic melts during fractional crystallization. *Geology* **34**, 85–88.

Ohmoto H., and Kerrick D. (1977) Devolatilization equilibria in graphitic systems. *Am. J. Sci.* **277**, 1013–1044.

Palenik C. S., Utsunomiya S., Reich M., Kesler S. E., Wang L., and Ewing R. C. (2004) "Invisible" gold revealed: direct imaging of gold nanoparticles in a Carlin-type deposit. *Am. Miner.* **89**, 1359–1366.

Pettke T., Heinrich C. A., Ciocan A. C., and Gunther D. (2000) Quadrupole mass spectrometry and optical emission spectroscopy: detection capabilities and representative sampling of short transient signals from laser-ablation. *J. Anal. Atom. Spectr.* **15**(9), 1149–1155.

Pettke T., Halter W. E., Webster J. D., Aigner-Torres M., and Heinrich C. A. (2004) Accurate quantification of melt inclusion chemistry by LA-ICPMS: a comparison with EMP and SIMS and advantages and possible limitations of these methods. *Lithos* **78**, 333–361.

Pokrovski G. S., Zakirov I. V., Roux J., Testemale D., Hazemann J.-L., Bychkov A. Y., and Golikova G. V. (2002a) Experimental study of arsenic speciation in vapor phase to 500C: implications for As transport and fractionation in low-density crustal fluids and volcanic gases. *Geochem. Cosmochim. Acta* **66**, 3453–3480.

Pokrovski G. S., Kara S., and Roux J. (2002b) Stability and solubility of arsenopyrite, FeAsS, in crustal fluids. *Geochim. Cosmochim. Acta* **66**, 2361–2378.

Price R. E., and Pichler T. (2005) Distribution, speciation and bioavailability of arsenic in a shallow-water submarine hydrothermal system, Tutum Bay, Ambitle Island, PNG. *Chem. Geol.* **224**, 122–135.

Quisefit J. P., Toutain J. P., Bergametti G., Javoy M., Cheynet B., and Person A. (1989) Evolution versus cooling of gaseous volcanic emissions from Momotombo Volcano, Nicaragua : thermochemical model and observations. *Geochim. Cosmochim. Acta* **53**, 2591–2608.

Richards J. P. (2005) Cumulative factors in the generation of giant calc-alkaline porphyry Cu deposits. In *Super Porphyry Copper and Gold Deposits—A Global Perspective*, vol. 1 (ed. T. M. Porter) PGC Publishing, Adelaide, pp. 7–25.

Richards J. P., McCulloch M. T., Chappell B. W., and Kerrich R. (1991) Sources of metals in the Porgera gold deposit, Papua New Guinea; evidence from alteration, isotope, and noble metal geochemistry. *Geochim. Cosmochim. Acta* **55**, 565–580.

Roedder E. (1972) Compositions of fluid inclusions. U.S. Geological Survey Professional Paper 440, 164 p.

Roedder E. (1984) Fluid inclusions. *Reviews in Mineralogy* **12**, 644.

Sasso A. M., and Clark A. H. (1998) The Farallon Negro group, northwestern Argentina: magmatic, hydrothermal and tectonic evolution and implications for Cu–Au metallogeny in the Andean back-arc. *Soc. Econ. Geol. Newsl.* **24**, 1–18.

Scaillet B., and MacDonald R. (2001) Phase relations of peralkaline silicic magmas and petrogenetic implications. *J. Petrol.* **42**, 825–845.

Shinohara H., and Kazahaya K. (1995) Degassing processes related to magma-chamber crystallization. In *Magmas, Fluids and Ore Deposits*, vol. 23 (ed. J. F. H. Thompson). Mineralogical Association of Canada Short Course, pp. 47–70.

Shinohara H., and Hedenquist J. W. (1997) Constraints on magma degassing beneath the Far Southeast porphyry Cu–Au deposit, Philippines. *J. Petrol.* **38**, 1741–1752.

Signorelli S., Buccianti A., Martini M., and Piccardi G. (1998) Arsenic in fumarolic gases of Vulcano (Aeolian Islands, Italy) from 1978 to 1993: geochemical evidence from multivariate analysis. *Geochem. J.* **32**, 367–382.

Sillitoe R. H. (1979) Some thoughts on gold-rich porphyry copper deposits. *Miner. Deposita* **14**, 161–174.

Sillitoe R. H. (1993a) Epithermal models: genetic types, geometric controls and shallow features; in ore deposits modeling. *Geolo. Assoc. Can.* **40**, 403–417.

Sillitoe R. H. (1993) Gold-rich porphyry copper deposits; geological model and exploration implications, In *Mineral Deposit Modeling*. Geological Society of Canada Special Paper, vol. 40, pp. 403–417.

Sillitoe R. H. (2000) Gold-rich porphyry deposits: descriptive and genetic models and their role in exploration and discovery. *Rev. Econ. Geol.* **13**, 315–345.

Simmons S. F., White N. C., and John D. A. (2005) Geological characteristics of epithermal. In *Econ. Geol. 100th Anniv. Vol.* (eds. J. W. Hedenquist, J. F. H. Thompson, R. J. Goldfarb, and J. P. Richards), pp. 485–522.

Simon G., Huang H., Penner-Hahn J. E., Kesler S. E., and Kao L. (1999) Oxidation state of gold and arsenic in gold-bearing arsenian pyrite. *Am. Miner.* **84**, 1071–1079.

Simon A. C., Frank M. R., Pettke T., Candela P. A., Piccoli P. M., Heinrich C. A., and Glascock M. (2007) An evaluation of synthetic fluid inclusions for the purpose of trapping equilibrated, coexisting, immiscible fluid phases at magmatic conditions. *Am. Miner* **92**, 124–138.

Simon A. C., Pettke T., Candela P. A., Piccoli P. M., and Heinrich C. A. (2006) Copper partitioning at magmatic conditions. *Geochim. Cosmochim. Acta* **70**, 5583–5600.

Simon A. C., Pettke T., Candela P. A., Piccoli P. M., and Heinrich C. A. (2005) Gold partitioning in melt–vapor–brine systems. *Geochim. Cosmochim. Acta* **69**, 3321–3335.

Simon A. C., Pettke T., Candela P. A., Piccoli P. M., and Heinrich C. A. (2004) Magnetite solubility and iron transport in magmatic-hydrothermal environments. *Geochim. Cosmochim. Acta* **68**, 4905–4914.

Simon A. C., Pettke T., Candela P. A., Piccoli P. M., and Heinrich C. A. (2003) Experimental determination of Au solubility in rhyolite melt and magnetite: constraints on magmatic Au budgets. *Am. Miner* **88**, 1644–1651.

Sourirajan S., and Kennedy G. C. (1962) The system NaCl–H_2O at elevated temperatures and pressures. *Am. J. Sci.* **260**, 115–141.

Sowerby J. R., and Keppler H. (1999) Water speciation in rhyolitic melt determined by in-situ infrared spectroscopy. *Am. Miner.* **84**, 1843–1849.

Stauffer R. E., and Thompson J. M. (1984) Arsenic and antimony in geothermal waters of Yellowstone National Park, Wyoming, USA. *Geochim. Cosmochim. Acta* **48**, 2547–2561.

Stefánsson A., and Seward T. M. (2003) Stability of chloridogold(I) complexes in aqueous solution from 300 to 600C and from 500 to 1800 bar. *Geochim. Cosmochim. Acta* **23**, 4559–4576.

Stefánsson A., and Seward T. M. (2004) Gold(I) complexing in aqueous sulphide solutions to 500 °C and 500 bar. *Geochim. Cosmochim. Acta* **68**, 4121–4143.

Sterner S. M., Hall D. L., and Bodnar R. J. (1989) Synthetic fluid inclusions. V. Solubility relations in the system NaCl–KCl–H_2O under vapor-saturated conditions. *Geochim. Cosmochim. Acta* **52**, 989–1005.

Sterner S. M., Chou I.-M., Downs R. T., and Pitzer K. S. (1992) Phase relations in the system NaCl–KCl–H_2O: V. Thermodynamic-PTX analysis of solid–liquid equilibria at high temperatures and pressures. *Geochim. Cosmochim. Acta* **56**, 2295–2309.

Stimac J., and Hickmott D. (1994) Trace-element partition-coefficients for Ilmenite, *ortho*-pyroxene and pyrrhotite in rhyolite determined by Micro-Pixe Analysis. *Chem. Geol.* **117**, 313–330.

Symonds R. B., Rose W. I., Reed M. H., Lichte F. E., and Finnean D. L. (1987) Volatilization transport and sublimation of metallic and non-metallic elements in high-temperature gases at Merapi Volcano, Indonesia. *Geochim. Cosmochim. Acta* **51**, 2083–2101.

Symonds R. B., Rose W. I., Gerlack T. M., Briggs P. H., and Harmon R. S. (1990) Evaluation of gases, condensates, and SO_2 emissions from Augustino volcano, Alaska: the degassing of a Cl-rich volcanic system. *Bull. Vocanol.* **52**, 355–374.

Symonds R. B., Reed M. H., and Rose W. I. (1992) Origin, speciation and fluxes of trace element gases at Augustine volcano, Alaska: insights into magma degassing and fumarolic processes. *Geochim. Cosmochim. Acta* **56**, 633–657.

Symonds R. B., Rose W. I., Bluth G., and Gerlach T. M. (1994) Volcanic gas studies: methods, results, and applications. In *Volatiles in Magmas*, vol. 30 (eds. M. R. Carroll and J. R. Holloway). Mineralogical Society of America Reviews in Mineralogy, pp. 1–66.

Tacker R. C., and Candela P. A. (1987) Partitioning of molybdenum between magnetite and melt; a preliminary experimental study of partitioning of ore metals between silicic magmas and crystalline phases. *Econ. Geol.* **82**(7), 1827–1838.

Taran Y. A., Hedenquist J. F., Korzhinsky M. A., Tkachenko S. I., and Shmulovich K. I. (1995) Geochemistry of magmatic gases from Kudryavy volcano, Iturup, Kuril islands. *Geochem. Cosmochim. Acta* **59**, 1749–1761.

Thompson R. N., and MacKenzie W. S. (1967) Feldspar-liquid equilibria in peralkaline acid liquids: an experimental study. *Am. J. Sci.* **265**, 714–734.

Titley S. R. (1981) Geological and geotectonic setting of porphyry copper deposits in the southern Cordillera. *Ariz. Geol. Soc.* **14**, 79–97.

Toulmin P., and Barton P. B. (1964) A thermodynamic study of pyrite and pyrrhotite. *Geochim. Cosmochim. Acta* **28**, 641–671.

Ulrich T., Günther D., and Heinrich C. A. (1999) Gold concentrations of magmatic brines and the metal budget of porphyry copper deposits. *Nature* **399**, 676–679.

Ulrich T., Günther D., and Heinrich C. A. (2001) Evolution of a porphyry Cu–Au deposit, based on LA-ICP-MS analysis of fluid inclusions, Bajo de la Alumbrera, Argentina. *Econ. Geol.* **97**, 1888–1920.

Van Leeuwen T. M., Leach T. M., Hawke M. M., and Hawke A. (1990) The Kelian disseminated gold deposit, East Kalimantan, Indonesia. *J. Geochem. Explor.* **35**, 1–61.

Vila T., and Sillitoe R. H. (1991) Gold-rich porphyry systems in the Maricunga Belt, northern Chile. *Econ. Geol.* **86**, 1238–1260.

Wall V. J. (1997) Bajo de la Alumbrera (Argentina). A world class copper gold deposit. *Rev. Assoc. Argentina Geol. Econ.* **11**, 92.

Watson E. B. (1994) Diffusion in volatile-bearing magmas. *Rev. Miner.* **30**, 371–411.

White D. (1981) Active geothermal systems and hydrothermal ore deposits. In *Econ. Geol. 75th Anniv. Vol.* (eds. B. Skinner), pp. 392–423.

Whitney J. W. (1975) Vapor generation in a quartz monzonite magma: a synthetic model with application to porphyry copper deposits. *Econ. Geol.* **70**, 346–358.

Williams T. J., Candela P. A., and Piccoli P. M. (1995) The partitioning of copper between silicate melts and two-phase aqueous fluids: an experimental investigation at 1 kilobar, 800 °C and 1/2 kilobar, 850 °C. *Contrib. Miner. Petrol.* **121**, 388–399.

Williams T. J., Candela P. A., and Piccoli P. M. (1997) Hydrogen-alkali exchange between silicate melts and two-phase aqueous mixtures; an experimental investigation. *Contrib. Miner. Petrol.* **128**, 114–126.

Williams-Jones A. E., Heinrich C. A., (2005). Vapor transport of metals and the formation of magmatic-hydrothermal ore deposits. *Econ. Geol. 100th Anniv. Vol.* (eds: J. W. Hedenquist, J. F. H. Thompson, R. J. Goldfarb, and J. P. Richards), pp. 1287–1312.

Ye Z., Kesler S. E., Essene E. J., Zohar P. B., and Borhauer J. L. (2003) Relation of Carlin-type mineralization to lithology, structure and alteration: Screamer zone, Betze-Post deposit, Nevada:. *Miner. Deposita* **38**, 22–38.

Yudovskaya M. A., Distler V. V., Chaplygin I. V., Mokhov A. V., Trubkin N. V., and Gorbacheva S. A. (2006) Gaseous transport and deposition of gold in magmatic fluid: evidence from the active Kudryavy volcano, Kurile islands. *Miner. Deposita* **40**, 828–848.

Associate editor: Edward M. Ripley